

# Frequency Modulated Gyroscopes

*Mitchell Kline*

Electrical Engineering and Computer Sciences  
University of California at Berkeley

Technical Report No. UCB/EECS-2015-26

<http://www.eecs.berkeley.edu/Pubs/TechRpts/2015/EECS-2015-26.html>

May 1, 2015



Copyright © 2015, by the author(s).  
All rights reserved.

Permission to make digital or hard copies of all or part of this work for personal or classroom use is granted without fee provided that copies are not made or distributed for profit or commercial advantage and that copies bear this notice and the full citation on the first page. To copy otherwise, to republish, to post on servers or to redistribute to lists, requires prior specific permission.

# Frequency Modulated Gyroscopes

by

Mitchell Kline

A dissertation submitted in partial satisfaction of the  
requirements for the degree of  
Doctor of Philosophy

in

Electrical Engineering and Computer Science

in the

Graduate Division

of the

University of California, Berkeley

Committee in charge:

Professor Bernhard E. Boser, Chair  
Professor Seth Sanders  
Professor Liwei Lin, Mechanical Engineering

Fall 2013

# Frequency Modulated Gyroscopes

Copyright 2013

by

Mitchell Kline

## Abstract

Frequency Modulated Gyroscopes

by

Mitchell Kline

Doctor of Philosophy in Electrical Engineering and Computer Science

University of California, Berkeley

Professor Bernhard E. Boser, Chair

MEMS gyroscopes for consumer devices, such as smartphones and tablets, suffer from high power consumption and drift which precludes their use in inertial navigation applications. Conventional MEMS gyroscopes detect Coriolis force through measurement of very small displacements on a sense axis, which requires low-noise, and consequently high-power, electronics. The sensitivity of the gyroscope is improved through mode-matching, but this introduces many other problems, such as low bandwidth and unreliable scale factor. Additionally, the conventional Coriolis force detection method is very sensitive to asymmetries in the mechanical transducer because the rate signal is derived from only the sense axis. Parasitic coupling between the drive and sense axis introduces unwanted bias errors which could be rejected by a perfectly symmetric readout scheme.

In this thesis, I present frequency modulated (FM) gyroscopes that overcome the above limitations. FM gyroscopes operate the mechanical transducer in a perfectly symmetric way: each transducer axis is continuously driven to maintain a constant envelope oscillation. The rate is detected as changes in the frequencies of oscillations of the two axes. Frequency readout offers superior scale factor reliability in comparison to amplitude readout. For pendulum type gyroscopes, the scale factor is a dimensionless constant equal to 1 Hz (or cycle per second) per 360 deg/s.

FM gyroscopes are trivial to mode-match. Oscillation frequencies of both axes can be continually monitored and matched through electrostatic tuning. The FM gyroscope receives the same improved sensitivity benefit from mode-matching as the conventional gyroscope, without the drawbacks of limited bandwidth or unreliable scale factor.

Because of the symmetry, compatibility with mode-matching, and ease of frequency readout, the FM gyroscopes promise to improve the power dissipation and drift of MEMS gyroscopes.

To my parents for their endless support.  
And to my wife for her patience and encouragement.

# Contents

<b>Contents</b>	<b>ii</b>
<b>List of Figures</b>	<b>iv</b>
<b>List of Tables</b>	<b>vi</b>
<b>1 Vibratory gyroscope model</b>	<b>8</b>
1.1 Two degree of freedom resonator . . . . .	8
1.2 Noise model for gyroscopes . . . . .	11
<b>2 Conventional rate gyroscope</b>	<b>13</b>
2.1 Phasor analysis . . . . .	13
2.2 Ideal gyroscope . . . . .	15
2.3 Gyroscope with direct damping terms . . . . .	17
2.4 Gyroscope with frequency mismatch . . . . .	18
2.5 Gyroscope with damping and frequency mismatch . . . . .	19
2.6 Gyroscope with cross-axis spring and damper coupling . . . . .	20
2.7 Noise in the mode-matched AM gyroscope . . . . .	21
2.8 Noise in the mismatched AM gyro . . . . .	22
2.9 Conclusion . . . . .	24
<b>3 QFM gyroscope</b>	<b>25</b>
3.1 QFM gyro concept . . . . .	26
3.2 Phasor analysis . . . . .	27
3.3 Ideal QFM gyroscope . . . . .	28
3.4 QFM gyroscope with frequency mismatch . . . . .	29
3.5 QFM gyroscope with mechanical cross coupling . . . . .	30
3.6 Noise in the FM gyroscope . . . . .	30
3.7 Dual QFM gyroscope . . . . .	33
3.8 Experimental Results . . . . .	35
3.9 Conclusion . . . . .	39
<b>4 Lissajous pattern gyroscope</b>	<b>41</b>

4.1	Ideal LFM gyroscope . . . . .	44
4.2	LFM gyroscope with mechanical cross coupling . . . . .	46
4.3	Noise in the LFM gyroscope . . . . .	47
4.4	AM readout of Lissajous gyroscope . . . . .	49
4.5	Impact of amplitude ripple . . . . .	50
4.6	Gyroscope test bench . . . . .	52
4.7	Dual mass gyroscope test chip . . . . .	54
4.8	Conclusion . . . . .	65
	<b>Bibliography</b>	<b>68</b>

# List of Figures

1.1	Two degree of freedom resonator. . . . .	8
3.1	QFM gyroscope concept illustrated by Foucault pendulum. . . . .	26
3.2	Circuit used for evaluating noise of QFM gyroscope. . . . .	31
3.3	Phase domain representation of circuit in Figure 3.2. . . . .	31
3.4	Layout diagram of ring gyroscope test-chip. . . . .	36
3.5	Photograph of ring gyroscope device. . . . .	37
3.6	Partial schematic of ring gyroscope electrode connections. . . . .	37
3.7	The QFM controller maintains equal velocity amplitude oscillations on each axis and additionally mode-matches the gyroscope. . . . .	38
3.8	Allan deviation comparison between single and dual QFM gyroscopes. . .	40
4.1	The trajectory of the proof mass when the x- and y-axis oscillators run at different frequencies creates a Lissajous pattern. . . . .	43
4.2	Circuit used for evaluating noise of LFM gyroscope. . . . .	47
4.3	Impact of amplitude ripple due to cross-axis spring coupling on LFM gyroscope. . . . .	51
4.4	Quadrature cancellation method also showing sustaining amplifiers. . . .	52
4.5	Demodulated complex envelope of frequencies after quadrature cancellation.	53
4.6	Photograph of gyroscope test bench. . . . .	53
4.7	Front panel of FPGA controller. . . . .	55
4.8	Representative frequency response of dual mass gyroscope. . . . .	56
4.9	Picture of 3.3 kcps pendular gyroscope fabricated by Invensense. . . . .	56
4.10	Die photo of test chip. . . . .	56
4.11	Layout diagram of 3.3 kcps pendular gyroscope fabricated by Invensense.	57
4.12	Partial schematic of readout electronics for 3 kcps pendular gyroscope. . .	57
4.13	Dual force-feedback gyroscope controller implementation. . . . .	59
4.14	Comparison of Allan Deviation for conventional force feedback and dual force feedback (Lissajous pattern) operating modes. . . . .	60
4.15	Conceptual implementation of LFM gyroscope. The split frequency controller is optional. . . . .	61

4.16	Conceptual implementation final LFM demodulation. The measured frequencies are further AM demodulated in order to form the bias-free rate estimate. . . . .	62
4.17	Uncalibrated output of gyroscope showing accurate scale factor of LFM operating mode. . . . .	62
4.18	Deviation from the ideal linear transfer curve in the LFM operating mode.	63
4.19	Bias and relative scale factor response to a temperature step in the open loop rate mode. The steps correspond to 20 K shifts. The bias coefficient is $11.2 \times 10^{-3} \text{ }^\circ/\text{s/K}$ , and the scale factor is 4100 ppm/K. . . . .	64
4.20	Bias and relative scale factor response to a temperature step in the LFM mode. The bias coefficient is $2.4 \times 10^{-3} \text{ }^\circ/\text{s/K}$ , and the scale factor is 27 ppm/K. . . . .	64
4.21	The long term bias over a few months is less than $\pm 60$ ppm relative to $1000 \text{ }^\circ/\text{s}$ , or $60 \times 10^{-3} \text{ }^\circ/\text{s}$ . . . . .	65
4.22	Scale factor variation over 3 days in the conventional AM operating mode.	66
4.23	Scale factor variation over 1 day in LFM operating mode. The x-axis scale is 6 hours per division. . . . .	67

# List of Tables

3.1	Ring gyroscope electrode functionality. . . . .	36
4.1	Comparison of scale factor and offset of AM and FM gyroscopes. . . . .	67

## Acknowledgments

I want to thank my advisor for keeping me pointed in the right direction; my lab-mates, for their friendship, feedback, and continuous stream of good ideas; my parents, for their unwavering support; and my wife, for her patience, encouragement, and understanding.

I would also like to acknowledge the Berkeley Sensor and Actuator Center and the Defense Advanced Research Projects Agency, without whose support none of this would have been possible.

# Foreword

## Organization of this thesis

The first 2 chapters of this thesis serve as a review on the basic theory of conventional vibratory gyroscope operation. Chapter 1 presents the vibratory gyroscope model which is often referred to throughout the text. Chapter 2 presents the open-loop sense operating mode in detail, going through the sources of offset, scale factor dependence, and noise.

Chapter 3 presents the QFM gyroscope and its derivatives. Sources of offset, scale factor instability, and noise are discussed and compared to the conventional gyroscopes of the earlier chapters.

Chapter 4 introduces the Lissajous FM gyroscope (LFM), which addresses a major shortcoming of the QFM gyroscope. The LFM gyroscope and its implementation are the primary focus of this thesis.

## Table of Commonly Used Symbols

Symbol	Dimension	Definition
$m$	mass	Resonator proof mass
$\mathbf{q}$	length	vector of proof mass displacements
$x$	length	x-axis proof mass displacement
$y$	length	y-axis proof mass displacement
$x_a$	length	amplitude of x-axis proof mass displacement
$y_a$	length	amplitude y-axis proof mass displacement
$\phi_x$	phase	phase of x-axis proof mass displacement
$\phi_y$	phase	phase of y-axis proof mass displacement
$\Delta\phi_{xy}$	phase	difference of x- and y-axis phase
$\dot{\phi}_x$	ang. freq.	instantaneous frequency of x-axis
$\dot{\phi}_y$	ang. freq.	instantaneous frequency of y-axis
$\Sigma\dot{\phi}_{xy}$	ang. freq.	sum of x- and y-axis instantaneous frequencies
$\Delta\dot{\phi}_{xy}$	ang. freq.	difference of x- and y-axis instantaneous frequencies
$x_c$	length	in-phase component of x-axis proof mass displacement
$y_c$	length	in-phase component of y-axis proof mass displacement
$x_s$	length	quadrature component of x-axis proof mass displacement
$y_s$	length	quadrature component of y-axis proof mass displacement
$\mathbf{K}$	stiffness	matrix of resonator stiffnesses
$k_x$	stiffness	x-axis resonator stiffness
$k_y$	stiffness	y-axis resonator stiffness
$\mathbf{C}$	damping	matrix of resonator damping
$c_x$	damping	x-axis resonator damping
$c_y$	damping	y-axis resonator damping
$\mathbf{F}$	force	vector of input forces to resonator
$F_x$	force	x-axis input force to resonator
$F_y$	force	y-axis input force to resonator
...		

Symbol	Dimension	Definition
...		
$F_{xc}$	force	in-phase component of x-axis force
$F_{yc}$	force	in-phase component of y-axis force
$F_{xs}$	force	quadrature component of x-axis force
$F_{ys}$	force	quadrature component of y-axis force
$\Omega$	ang. freq.	matrix of input angular rates
$\Omega_z$	ang. freq.	z-axis input angular rate
$\alpha_z$	1	mechanical angular gain factor
$\omega_{ox}$	ang. freq.	resonant frequency of x-axis
$\omega_{oy}$	ang. freq.	resonant frequency of y-axis
$\omega_c$	aang. freq.	zero rate circular orbit frequency
$\beta_x$	ang. freq.	bandwidth of resonator x-axis
$\beta_y$	ang. freq.	bandwidth of resonator y-axis
$\Omega_k\{x, y\}$	ang. freq.	quadrature (cross-spring) error
$\Omega_c$	ang. freq.	cross-damper error
$v_x$	velocity	x-axis proof mass velocity
$v_y$	velocity	y-axis proof mass velocity
$v_{xa}$	velocity	amplitude of x-axis proof mass velocity
$v_{ya}$	velocity	amplitude y-axis proof mass velocity
$S_\Omega(\omega)$	ang. freq.	rate noise PSD at frequency $\omega$
$\sigma_\Omega^2(\tau)$	(ang. freq.) <sup>2</sup>	Allan variance with averaging time $\tau$
$h_0$	ang. freq.	white component of $S_\Omega(\omega)$
$h_{-1}$	(ang. freq.) <sup>2</sup>	1/f component of $S_\Omega(\omega)$
$h_{-2}$	(ang. freq.) <sup>3</sup>	1/f <sup>2</sup> component of $S_\Omega(\omega)$
$\gamma_o$	1	ratio of white electronics noise to Brownian noise
$\Delta r_v$	1	difference of reciprocal velocity amplitude ratios
$\Sigma r_v$	1	sum of reciprocal velocity amplitude ratios

## A note about frequency notation and units

The SI system defines the Hertz as the reciprocal second, or  $1 \text{ Hz} = \text{s}^{-1}$ , but the radian per second has just as good (or better) of a claim to  $\text{s}^{-1}$  due to how the trigonometric functions are defined. To avoid this problem, I will use the unit of angular (or phase) velocity  $\text{cps} = 1 \text{ cycle/s}$ . Cycles are natural to think about in terms of physically rotating objects, such as a record on a turntable (or what a gyroscope measures), but the same definition can be applied to more abstract concepts, such as the phase of a sinusoid. A record spinning at  $1 \text{ turn/s}$  has an angular velocity of  $1 \text{ cps}$ , and a sinusoid with a period of  $1 \text{ s}$  has a phase velocity, or frequency, of  $1 \text{ cps}$ . The cps can be defined by any of the following (or any of their derivatives)

$$1 \text{ cps} = 1 \text{ cycle/s} = 1 \text{ c/s} = 1 \text{ turn/s} = 360^\circ/\text{s} = 2\pi \text{ rad/s}, \quad (0.1)$$

where  $c$  is a unit of angle equal to 1 full turn.<sup>1</sup> Furthermore, the radian will *always* be treated as a dimensionless number with  $1 \text{ rad} = 1$ .<sup>2</sup> As such, the radian will occasionally be dropped from expressions where it has no meaning, e.g., the derivative of a sinusoidal charge variation on a capacitor with a period of  $1 \text{ s}$  becomes

$$\begin{aligned} \frac{d}{dt} 1 \text{ C} \sin(1 \text{ cps} \times t) &= 1 \text{ cps} \times 1 \text{ C} \cos(1 \text{ cps} \times t) \\ &= 2\pi \frac{\text{rad}}{\text{s}} 1 \text{ C} \cos(1 \text{ cps} \times t) = 2\pi \text{ A} \cos(1 \text{ cps} \times t). \end{aligned} \quad (0.2)$$

The above notation might look slightly disturbing: there are no  $2\pi$  factors in the arguments to the sines and cosines. But, using the definition of cps, we find

$$\sin(1 \text{ cps} \times t) = \sin\left(2\pi \frac{\text{rad}}{\text{s}} \times t\right). \quad (0.3)$$

The  $\text{s}^{-1}$  will cancel when multiplied by  $t$  and the sine function receives its argument in radians, as it expects.

---

<sup>1</sup>The usage of the symbol  $c$  for cycle is suggested by [1].

<sup>2</sup>This definition of the radian can alternatively be thought of as all angles are measured relative to  $1 \text{ rad}$ , or that all angles are specified as a ratio of arc length to radius. If we instead chose to treat the radian as a real dimension, we would have to write all calls to trig functions with the form  $\sin\left(\frac{\theta}{1 \text{ rad}}\right)$ , where  $\theta$  is an angle.

I will use the convention of notating angular velocities with  $\Omega$  and phase velocities with  $\omega$ . For example, the angular velocity of a record on a turntable is given as

$$\Omega_o = 33\frac{1}{3} \text{ rpm} = \frac{5}{9} \text{ cps}, \quad (0.4)$$

and the natural frequency of a resonator would be given as

$$\omega_o = 1 \text{ kcps} = 2\pi \times 1 \text{ krad/s}, \quad (0.5)$$

meaning the system would oscillate with a period of 1 ms. I will not use the unit Hz, as it is tempting to replace it by  $\text{s}^{-1}$ , violating my claim to treat  $\text{rad/s} = \text{s}^{-1}$ .

There is one problematic area in electrical engineering where the reciprocal second is used in an ambiguous way: noise specification. The formula for the noise voltage power spectral density (PSD) of a resistor with value  $R$  is

$$S_V = 4kTR. \quad (0.6)$$

In the SI system, the units of the above are  $\text{V}^2/\text{s}^{-1}$ , which are presumed to be equal to  $\text{V}^2/\text{cps}$ . This goes against the convention I have specified above, but there is an easy fix. I will explicitly write out the PSD formulas in the form

$$S_V = 4kTR/c. \quad (0.7)$$

The units are now unambiguously  $\text{V}^2\text{s}/c$  or  $\text{V}^2/\text{cps}$ . This does not break the old system: if the unit  $c$  is treated as 1—the implicit assumption in the original formula—the modified formula gives the correct answer in  $\text{V}^2/\text{cps}$ . The only possible way to make a mistake is to have interpreted the units of  $s$  as  $\text{s}/\text{rad}$ , introducing an incorrect scale factor when converting to  $1/\text{cps}$ .

Why go to all this trouble? Using the above convention will save the tediousness of having to use different variables for “normal” and angular frequencies, or alternatively, having hundreds of  $2\pi$  factors scattered throughout the text. The former benefit is especially nice for specification of the FM gyroscope, which works by adding an input angular velocity to the natural frequency of the gyroscope. It is also fully compatible with computer algebra systems that keep track of units, such as Mathcad. Finally,

it prevents mistakes by extending unit-label analysis to include angle and frequency units: there is no ambiguity about whether  $1 \text{ rad} = 1$  or  $1 \text{ c} = 1$ . One could argue that the latter choice would be the right one, but it would require changing the definition of all of the trig functions.<sup>3</sup>

## Gyro noise specification

The IEEE has defined a standard noise specification for gyroscopes as

$$S_{\Omega}(f) = N^2 + \frac{B^2}{2\pi f} + \frac{K^2}{(2\pi f)^2}, \quad (0.8)$$

where  $S_{\Omega}(f)$  is the double sided rate noise power spectral density (PSD),  $f$  is in cps, and  $N$ ,  $B$ , and  $K$  are coefficients representing the angle random walk, bias stability, and rate-random walk of the gyroscope, respectively [2]. There are a couple of issues with this PSD format that have created confusion when specifying and comparing noise performance of gyroscopes. The first is that this is a double-sided PSD, whereas what a spectrum analyzer measures is the single-sided PSD. We can define the single-sided PSD as

$$G_{\Omega}(f) = 2 \left( N^2 + \frac{B^2}{2\pi f} + \frac{K^2}{(2\pi f)^2} \right). \quad (0.9)$$

The second issue is the inclusion of the  $2\pi$  factors in the PSD specification. This is in contrast to how oscillators are usually specified [3], with

$$S_y(f) = h_0 + \frac{h_{-1}}{f} + \frac{h_{-2}}{f^2}, \quad (0.10)$$

where  $S_y(f)$  is the single-sided PSD. The oscillator specification is more natural, as PSDs are normally specified in  $\text{unit}^2/\text{cps}$ , meaning that the units of  $h_{-1}$  are simply  $\text{unit}^2$ . The  $2\pi$  factors in the IEEE definition seem to imply that the coefficient of the  $1/f$  term should be scaled in such a way that when divided by a frequency specified in  $\text{rad/s}$ , the final result will be per unit cps.

---

<sup>3</sup>Or treating angles as physical dimensions.

Because of the above points, I will use the convention defined by (0.10). The  $N$ ,  $B$ , and  $K$  parameters defined by the IEEE gyro standard can be found with<sup>4</sup>

$$N^2 = \frac{h_0}{2} \quad (0.11)$$

$$B^2 = \pi h_{-1} \quad (0.12)$$

$$K^2 = 2\pi^2 h_{-2}. \quad (0.13)$$

Gyroscope noise can also be specified by the Allan deviation. The IEEE standard defines the relationship between the PSD and Allan variance with

$$\sigma_{\Omega}^2(\tau) = \frac{N^2}{\tau} + \frac{2 \ln 2 B^2}{\pi} + \frac{K^2 \tau}{3}. \quad (0.14)$$

Substituting in the  $h_{\alpha}$  terms above, the Allan variance is

$$\sigma_y^2(\tau) = \frac{1}{2} \frac{h_0}{\tau} + 2 \ln 2 h_{-1} + \frac{2\pi^2 \tau}{3} h_{-2}, \quad (0.15)$$

which is in agreement with the expression used for oscillators.

There is one minor issue with the above expression for Allan variance related to the ambiguity of the reciprocal second: if  $N$  (or  $h_0$ ) is specified in deg/s/ $\sqrt{\text{cps}}$ , the cps is to be interpreted as  $s^{-1}$  according to convention. Similar to the noise example in the previous section, we can define

$$\sigma_{\Omega}^2(\tau) = \frac{N^2}{\tau} \text{c} + \frac{2 \ln 2 B^2}{\pi} + \frac{K^2 \tau}{3\text{c}} \quad (0.16)$$

$$\sigma_y^2(\tau) = \frac{1}{2} \frac{h_0}{\tau} \text{c} + 2 \ln 2 h_{-1} + \frac{2\pi^2 \tau}{3\text{c}} h_{-2}. \quad (0.17)$$

Again, this does not break the original definitions where the assumption  $1 \text{ c} = 1$  was made implicitly, it only enables the unambiguous interpretation of the reciprocal second.

The two single-sided PSDs and two expressions for Allan variances are equal, i.e.,  $G_{\Omega}(f) = S_y(f)$  and  $\sigma_{\Omega}^2(\tau) = \sigma_y^2(\tau)$ . The only change is how the coefficients of the frequency components are specified.

---

<sup>4</sup>When converting to the IEEE definition, it is best to retain the cps units, i.e., do not convert the result to  $^{\circ}/\sqrt{\text{s}}$  but leave it in  $^{\circ}/\text{s}/\sqrt{\text{cps}}$ . Replacing the cps may cause confusion to the reader: should they interpret the s as s/rad or s/cycle?

# Chapter 1

## Vibratory gyroscope model

### 1.1 Two degree of freedom resonator

A vibratory gyroscope is a 2 degree of freedom (DOF) resonator modeled by the system of Figure 1.1. The system consists of a mass  $m$ , springs  $k_1$  and  $k_2$ , and

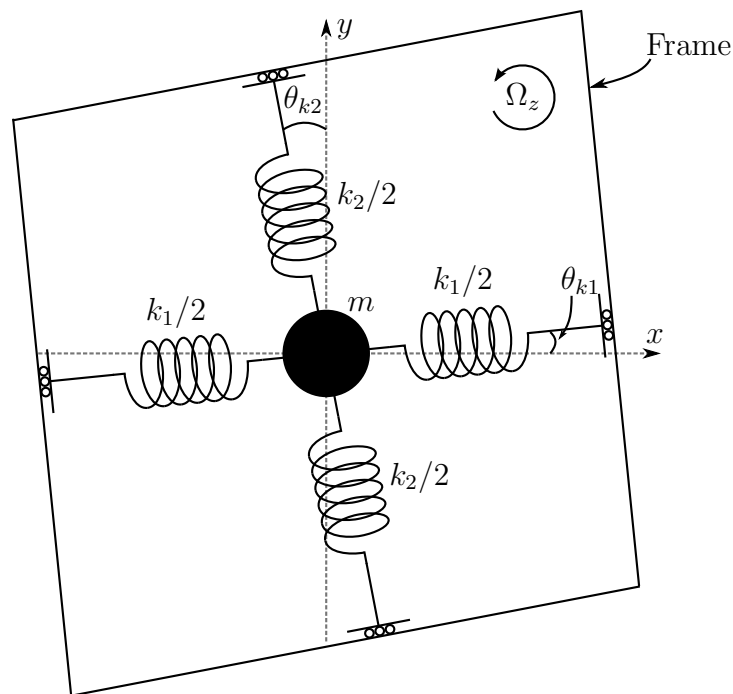


Figure 1.1: Two degree of freedom resonator.

dampers  $c_1$  and  $c_2$  (not shown but connected similarly to the springs). To capture an effect due to fabrication imperfections, the springs  $k_1$  and  $k_2$  are offset by angles  $\theta_{k1}$  and  $\theta_{k2}$  from the true  $x$  and  $y$  axes. Similarly, the dampers are offset by angles  $\theta_{c1}$  and  $\theta_{c2}$ . The true  $x$  and  $y$  axes indicate the directions in which motion is sensed and forces are applied. The  $x$  and  $y$  axes are rigidly attached to the frame, i.e., when the frame rotates, the axes rotate with them.

The equation of motion of this system in the rotating frame is

$$m\ddot{\mathbf{q}} + (2\boldsymbol{\Omega} + \mathbf{C})\dot{\mathbf{q}} + \mathbf{K}\mathbf{q} = \mathbf{F}. \quad (1.1)$$

where  $\mathbf{q} = \begin{bmatrix} x & y \end{bmatrix}^\top$  is the 2-dimensional vector of axis displacements,

$$\boldsymbol{\Omega} = \begin{bmatrix} 0 & -\alpha_z \Omega_z \\ \alpha_z \Omega_z & 0 \end{bmatrix}$$

is a matrix containing the input rate,  $\mathbf{C}$  is matrix containing the resonator damping terms,  $\mathbf{K}$  is a matrix containing the resonator stiffness terms, and  $\mathbf{F} = \begin{bmatrix} F_x & F_y \end{bmatrix}^\top$  is the vector of input forces. The parameter  $\alpha_z$  is a dimensionless scale factor that models the angular slip factor of the gyroscope. The centrifugal force and rate derivative terms will be ignored in this analysis, as their effect is small relative to the first order error sources.

Ideally, the  $\mathbf{K}$  and  $\mathbf{C}$  matrices are diagonal, with all stiffnesses equal and all dampers equal to zero. This happens when  $\theta_{k1} = \theta_{k2} = 0$ ,  $k_1 = k_2$ ,  $\theta_{c1} = \theta_{c2} = 0$ , and  $c_1 = c_2 = 0$ . In this case, the only coupling between the equations in system (1.1) is due to the angular rate. The off-diagonal terms in  $\mathbf{K}$  and  $\mathbf{C}$  contribute additional coupling between the axes that typically results in bias error.

In general, the stiffness and damping matrices  $\mathbf{K}$  and  $\mathbf{C}$  are given by

$$\mathbf{K} = \begin{bmatrix} k_x & k_{xy} \\ k_{xy} & k_y \end{bmatrix} \text{ with} \quad (1.2)$$

$$k_x = k_1 \cos^2 \theta_{k1} + k_2 \sin^2 \theta_{k2} \quad (1.3)$$

$$k_y = k_2 \cos^2 \theta_{k2} + k_1 \sin^2 \theta_{k1} \quad (1.4)$$

$$k_{xy} = k_1 \cos \theta_{k1} \sin \theta_{k1} - k_2 \cos \theta_{k2} \sin \theta_{k2} \quad (1.5)$$

$$\mathbf{C} = \begin{bmatrix} c_x & c_{xy} \\ c_{xy} & c_y \end{bmatrix} \text{ with} \quad (1.6)$$

$$c_x = c_1 \cos^2 \theta_{c1} + c_2 \sin^2 \theta_{c2} \quad (1.7)$$

$$c_y = c_2 \cos^2 \theta_{c2} + c_1 \sin^2 \theta_{c1} \quad (1.8)$$

$$c_{xy} = c_1 \cos \theta_{c1} \sin \theta_{c1} - c_2 \cos \theta_{c2} \sin \theta_{c2}. \quad (1.9)$$

These matrices are guaranteed to be symmetric and positive definite.

The resonant frequencies  $\omega_{ox}$  and  $\omega_{oy}$  and bandwidths  $\beta_x$  and  $\beta_y$  of the  $x$  and  $y$  axes are given by

$$\omega_{ox} = \sqrt{\frac{k_x}{m}} \quad (1.10)$$

$$\omega_{oy} = \sqrt{\frac{k_y}{m}} \quad (1.11)$$

$$\beta_x = \frac{c_x}{2m} \quad (1.12)$$

$$\beta_y = \frac{c_y}{2m}. \quad (1.13)$$

Additionally, the quantities

$$\Omega_c = \frac{c_{xy}}{2m} \quad (1.14)$$

$$\Omega_{kx} = \frac{1}{2} \frac{k_{xy}}{\omega_{ox} m} \quad (1.15)$$

$$\Omega_{ky} = \frac{1}{2} \frac{k_{xy}}{\omega_{oy} m} \quad (1.16)$$

will appear frequently in the analysis of the gyroscope. The quantities  $\Omega_c$  and  $\Omega_{k\{x,y\}}$  will be shown to be the bias errors due to damper and spring axis misalignment,

respectively. With the small angle approximation, the above parameters reduce to

$$\Omega_c \approx \frac{c_1\theta_{c1} - c_2\theta_{c2}}{2m} \quad (1.17)$$

$$\Omega_{kx} \approx \frac{1}{2}\omega_{ox} \left( \theta_{k1} - \frac{k_2}{k_1}\theta_{k2} \right) \quad (1.18)$$

$$\Omega_{ky} \approx \frac{1}{2}\omega_{oy} \left( \frac{k_1}{k_2}\theta_{k1} - \theta_{k2} \right), \quad (1.19)$$

where the latter two equations show that devices with high resonant frequency are more sensitive to axis misalignment.

## 1.2 Noise model for gyroscopes

Thermal noise and drift are the ultimate limiting factors in gyroscope performance. The rate noise and random drift can be specified by a power spectral density (PSD) of the form

$$S_\Omega(\omega) = h_0 + \frac{h_{-1}}{\omega} + \frac{h_{-2}}{\omega^2}, \quad (1.20)$$

where  $h_0$  is the angle random walk, typically specified in  $(^\circ/\text{s}/\sqrt{\text{cps}})^2$ ,  $h_{-1}$  is the bias stability, typically in  $(^\circ/\text{hr})^2$ , and  $h_{-2}$  is the rate random walk, typically in  $(^\circ/\text{hr}\sqrt{\text{cps}})^2$  [3]. The noise can be characterized through Allan variance measurements. The 2-sample Allan variance is defined as half the expected squared difference between consecutive rate samples averaged over time  $\tau$ , or

$$\sigma_\Omega^2(\tau) = \frac{1}{2} \left\langle \left[ \bar{\Omega}(t_o, \tau) - \bar{\Omega}(t_o + t, \tau) \right]^2 \right\rangle, \quad (1.21)$$

where  $\bar{\Omega}(t_o, \tau) = \frac{1}{\tau} \int_{t_o}^{t_o+\tau} \Omega(t) dt$  and  $t_o$  is an arbitrary starting time. The relationship between the Allan variance and PSD is given by

$$\sigma_\Omega^2(\tau) = \frac{1}{2} \frac{h_0 c}{\tau} + \underbrace{2 \ln 2}_{\approx 1.39} h_{-1} + \underbrace{\frac{2\pi^2}{3}}_{\approx 6.58} \frac{h_{-2}}{c} \tau. \quad (1.22)$$

If the gyroscope is used as a whole angle sensor rather than an angular rate sensor, the angle noise can be reported as the integrated angular rate noise, or in the frequency domain,

$$S_\theta(\omega) = \frac{S_\Omega(\omega)}{\omega^2} = \frac{h_0}{\omega^2} + \frac{h_{-1}}{\omega^3} + \frac{h_{-2}}{\omega^4}. \quad (1.23)$$

The 2-sample Allan variance is not convergent for  $1/\omega^3$  and  $1/\omega^4$  noise components, so a 3-sample variance must be used when dealing with whole angle data [4]. The 3 sample Hadamard variance is defined as

$$\sigma_H^2(\tau) = \left\langle \left[ [\bar{\theta}(t_o, \tau) - \bar{\theta}(t_o + t, \tau)] - [\bar{\theta}(t_o + t, \tau) - \bar{\theta}(t_o + 2t, \tau)] \right]^2 \right\rangle, \quad (1.24)$$

where  $\bar{\theta}(t_o, \tau) = \frac{1}{\tau} \int_{t_o}^{t_o+\tau} \theta(t) dt$  is a sample of angle data over time  $\tau$  starting at time  $t_o$ . The Hadamard variance represents the expected squared difference of a difference of angle samples. As an example, if  $\sigma_H(1 \text{ hr}) = 1^\circ$ , and we recorded 3 consecutive angle samples each averaged for an hour, the difference between the difference of sample 1 and 2 and the difference of sample 2 and 3 is expected to be  $1^\circ$ . The relationship between the Hadamard variance and the PSD is

$$\sigma_H^2(\tau) = \frac{c}{2} h_0 \tau + \left( \underbrace{\frac{27}{4} \ln(3) - 8 \ln(2)}_{\approx 1.87} \right) h_{-1} \tau^2 + \underbrace{\frac{11\pi^2}{10}}_{\approx 10.86} \frac{h_{-2}}{c} \tau^3. \quad (1.25)$$

## Chapter 2

# Conventional rate gyroscope

In the conventional rate gyroscope [5–11], an input angular rate causes energy transfer from the drive mode of the gyro to the sense mode. The rate signal is read out as small amplitude changes of the sense axis. We will refer to this type of readout as the amplitude modulated (AM) gyroscope. The AM gyroscope is asymmetric. The drive and sense axes are often intentionally mismatched to extend the bandwidth and stabilize the scale factor of the measurement. The typical AM gyroscope consists of an oscillator with amplitude control around the drive axis and a high gain amplifier with synchronous AM demodulator for the sense axis.

### 2.1 Phasor analysis

Equation 1.1 is used to describe the operation of the AM gyroscope. Because gyroscopes are narrowband systems, the solution to the above differential equation will be nearly sinusoidal oscillations with frequency near the natural frequency of the device. This implies that we can use sinusoidal phasor analysis to solve the system.<sup>1</sup>

To begin, we assume the solution to the 2 DOF variety of the system is

$$\mathbf{q}(t) = \begin{bmatrix} x_a(t)e^{j\phi_x(t)} \\ (y_c(t) + jy_s(t))e^{j\phi_x(t)} \end{bmatrix}, \quad (2.1)$$

---

<sup>1</sup>This technique is also known to as the “method of averaging.” [12] The real part of the right hand side of the equation is the physical displacement signal. For brevity, I omit this operator and solve the complex form of the differential equation.

where  $x_a$  is the displacement amplitude of the  $x$ -mode,  $y_c$  and  $y_s$  are the cosine and sine components of the displacements of the  $y$ -mode relative to the  $x$ -mode, and  $\phi_x(t)$  is the phase of the  $x$ -mode, nearly equal to  $\omega_{ox}t$ . Differentiating Equation 2.1, we find

$$\dot{\mathbf{q}}(t) = \begin{bmatrix} \left( j\dot{\phi}_x(t)x_a(t) + \dot{x}_a(t) \right) e^{j\phi_x(t)} \\ \left( j\dot{\phi}_x(t)[y_c(t) + jy_s(t)] + \dot{y}_c(t) + j\dot{y}_s(t) \right) e^{j\phi_x(t)} \end{bmatrix}. \quad (2.2)$$

Because  $\dot{\phi}_x(t) \approx \omega_{ox}$ , we can assume  $\dot{\phi}_x(t)x_a(t) \gg \dot{x}_a(t)$ . In other words  $\dot{x}_a(t)$  is slowly varying relative to the resonant frequency of the system. With this approximation,

$$\dot{\mathbf{q}}(t) \approx \begin{bmatrix} j\dot{\phi}_x(t)x_a(t)e^{j\phi_x(t)} \\ j\dot{\phi}_x(t)[y_c(t) + jy_s(t)]e^{j\phi_x(t)} \end{bmatrix}. \quad (2.3)$$

Solving for  $\ddot{\mathbf{q}}$  and making the above assumption,

$$\ddot{\mathbf{q}}(t) \approx \begin{bmatrix} e^{j\phi_x(t)} \left( -\dot{\phi}_x^2(t)x_a(t) + j2\dot{\phi}_x(t)\dot{x}_a(t) \right) \\ e^{j\phi_x(t)} \left( -\dot{\phi}_x^2(t)y_c(t) + j2\dot{\phi}_x(t)\dot{y}_c(t) - \dot{\phi}_x^2(t)y_s(t) - j2\dot{\phi}_x(t)\dot{y}_s(t) \right) \end{bmatrix}, \quad (2.4)$$

where the resulting  $\ddot{\phi}_x(t)$ ,  $\ddot{x}_a(t)$ ,  $\ddot{y}_c(t)$ , and  $\ddot{y}_s(t)$  terms are ignored. The force used to drive the system is

$$\mathbf{F}(t) = \begin{bmatrix} F_{xa}(t)e^{j\phi_F(t)} \\ (F_{yc}(t) + jF_{ys}(t))e^{j\phi_F(t)} \end{bmatrix}, \quad (2.5)$$

where  $F_{xa}$  is the amplitude of the  $x$ -axis force,  $\phi_F$  is the phase of the force,  $F_{yc}$  is the cosine component of the  $y$ -axis force, and  $F_{ys}$  is the sine component of the  $y$ -axis force.

The assumed solutions (2.1, 2.3, 2.4) are substituted into (1.1). The resulting system of two complex equations are separated into real and imaginary parts, giving a set of four real equations and four unknowns:  $\dot{x}_a$ ,  $\dot{\phi}_x$ ,  $\dot{y}_c$ , and  $\dot{y}_s$ . The unknowns

form system of first order nonlinear ODEs,

$$\dot{x}_a = -\beta_x x_a + (\alpha_z \Omega_z - \Omega_c) y_c - \Omega_{kx} y_s - \frac{1}{2m\omega_{ox}} F_{xa} \sin \Delta\phi_x \quad (2.6)$$

$$\dot{\phi}_x = \omega_{ox} + \Omega_{kx} \frac{y_c}{x_a} - \frac{1}{2m\omega_{ox} x_a} F_{xa} \cos \Delta\phi_x \quad (2.7)$$

$$\dot{y}_c = -\beta_y y_c + \Delta\omega_o y_s - (\Omega_c + \alpha_z \Omega_z) x_a + \frac{1}{2m\omega_{ox}} F_{ys} \quad (2.8)$$

$$\dot{y}_s = -\beta_y y_s - \Delta\omega_o y_c + \Omega_{kx} x_a - \frac{1}{2m\omega_{ox}} F_{yc}, \quad (2.9)$$

where  $\Delta\omega_o = \frac{1}{2\omega_{ox}} (\omega_{ox}^2 - \omega_{oy}^2)$  and  $\Delta\phi_x = \phi_x - \phi_F$ . There were a number of simplifications made to obtain the above equations, including:

1.  $y_c, y_s \ll x_a$
2.  $\omega_{ox} \gg \Omega_c, \Omega_z$
3.  $\dot{\phi}_x$  terms in (2.6, 2.8, 2.9) are ignored.

## 2.2 Ideal gyroscope

The AM gyroscope operation is most easily understood when starting with an ideal model. The ideal, mode-matched gyroscope is defined by

$$\mathbf{K} = k\mathbf{I} \quad (2.10)$$

$$\mathbf{C} = \mathbf{0}. \quad (2.11)$$

Let  $\omega_o^2 = k/m$ , then equations 2.6–2.9 then reduce to

$$\dot{x}_a = \alpha_z \Omega_z y_c - \frac{1}{2m\omega_{ox}} F_{xa} \sin \Delta\phi_x \quad (2.12)$$

$$\dot{\phi}_x = \omega_o - \frac{1}{2m\omega_{ox} x_a} F_{xa} \cos \Delta\phi_x \quad (2.13)$$

$$\dot{y}_c = -\alpha_z \Omega_z x_a + \frac{1}{2m\omega_{ox}} F_{ys} \quad (2.14)$$

$$\dot{y}_s = -\frac{1}{2m\omega_{ox}} F_{yc}. \quad (2.15)$$

The ideal gyroscope is first driven into an oscillation on the drive axis, in this case,  $x$ . The amplitude of the oscillation is controlled with the  $F_{xa}$  input. The phase of the applied force should be orthogonal to the phase of the sensed  $x$ -axis displacement, i.e.,  $\Delta\phi_x = -90^\circ$ . The oscillation can be sustained with either a constant applied force, as in the case of a square wave drive, or with an amplitude feedback loop that controls  $x_a$  to a constant value. For now, we will assume the latter situation and define  $x_a = x_{ao}$ ; thus,  $\dot{x}_a = 0$ .

Ideally, no component of force  $F_{xa}$  would be applied to the phase equation (2.13). In practice, phase shifts introduced by the particular type of oscillator loop used could introduce this unwanted force component that will act to disturb the oscillation phase. Here, we assume an ideal oscillator that guarantees  $\Delta\phi_x = 90^\circ$ , and the frequency of oscillation is exactly  $\dot{\phi}_x = \omega_o$ .

Equations 2.14 and 2.15 define the dynamics of the sense axis. In the open-loop sense, AM gyroscope, the  $F_{yc}$  and  $F_{ys}$  force inputs are unused. This gives

$$\dot{y}_c = -\alpha_z \Omega_z x_a \quad (2.16)$$

$$\dot{y}_s = 0. \quad (2.17)$$

These equations indicate that the rate can be inferred from the component of the  $y$ -axis displacement in-phase with the  $x$ -axis displacement,  $y_c$ . The component  $y_c$  can be demodulated by multiplying the  $y$ -axis displacement by the a clock in phase with the  $x$ -axis displacement and low pass filtering. If  $x_a$  is measured in addition to  $y_c$ , we can form a ratiometric measurement to improve the stability of the scale factor. These equations also reveal that the input rate is integrated during the measurement process, that is

$$\frac{y_c}{x_a}(t) = -\alpha_z \left( \int_0^t \Omega_z(\tau) d\tau + \theta_o \right), \quad (2.18)$$

where  $\theta_o$  is the initial angle orientation of the gyroscope. Defining  $\theta(t) = \int_0^t \Omega_z(\tau) d\tau$ , we have

$$\frac{y_c}{x_a}(t) = -\alpha_z (\theta(t) + \theta_o), \quad (2.19)$$

which shows that this operating mode results in a direct measurement of the angle that the device has rotated through rather than the angular rate. The reason for

the rate-integration is that we have not included any damping in our ideal gyroscope analysis. Even if we had an ideal gyroscope, this operating mode would still be terribly impractical. If there is a DC component of the input rate, the  $y$ -axis amplitude will go toward infinity, which is clearly impossible for any practical device. The next section includes the effect of damping and arrives at the well-known result for an open-loop, mode-matched AM rate gyroscope.

## 2.3 Gyroscope with direct damping terms

The sense-axis behavior of the mode-matched gyroscope changes dramatically when we include direct damping terms. Let

$$\mathbf{C} = \begin{bmatrix} c_x & 0 \\ 0 & c_y \end{bmatrix}, \quad (2.20)$$

then

$$\dot{y}_c = -\beta_y y_c - \alpha_z \Omega_z x_a \quad (2.21)$$

$$\dot{y}_s = -\beta_y y_s. \quad (2.22)$$

The solution  $y_c$  is most easily found in the frequency domain. The Laplace transform gives

$$\frac{y_c}{x_a}(s) = -\frac{\alpha_z}{\beta_y} \frac{\Omega_z(s)}{s/\beta_y + 1}. \quad (2.23)$$

The  $y$ -axis displacement signal is now proportional to the input-rate rather than the input angle. The scale factor is inversely proportional to the bandwidth of the sense axis, which also sets the overall measurement bandwidth. This is problematic: if we decrease the bandwidth to get a larger scale factor, we lose all of our measurement bandwidth.

Another issue is that this is only true when the resonant frequencies of the gyroscope are perfectly matched. Small variations in the resonant frequencies can introduce huge variability in the scale factor. It is extremely difficult to enforce this mode-matched condition, as the sense-axis dynamics are not directly observable due to the energy in the axis being close to zero. To overcome these problems, AM gyroscopes are typically operated with an intentionally introduced frequency mismatch.

## 2.4 Gyroscope with frequency mismatch

AM gyroscopes are typically designed with an intentional frequency mismatch between the axes. This gives the advantage of stable scale factor and large bandwidth. The disadvantage is that the scale factor is much smaller than it is in the mode-matched case, which gives a noise penalty. To analyze this case, let

$$\mathbf{C} = \mathbf{0} \quad (2.24)$$

$$\mathbf{K} = \begin{bmatrix} k_x & 0 \\ 0 & k_y \end{bmatrix}. \quad (2.25)$$

Equations (2.8, 2.9) reduce to

$$\dot{y}_c = \Delta\omega_o y_s - \alpha_z \Omega_z x_a \quad (2.26)$$

$$\dot{y}_s = -\Delta\omega_o y_c. \quad (2.27)$$

Taking a Laplace transform and solving for  $y_c(s)$  and  $y_s(s)$ , we obtain

$$\frac{y_c}{x_a}(s) = -\frac{\alpha_z}{\Delta\omega_o^2} \frac{s}{\frac{s^2}{\Delta\omega_o^2} + 1} \Omega_z(s) \quad (2.28)$$

$$\frac{y_s}{x_a}(s) = \frac{\alpha_z}{\Delta\omega_o} \frac{1}{\frac{s^2}{\Delta\omega_o^2} + 1} \Omega_z(s). \quad (2.29)$$

Notice that there is no DC rate sensitivity in the  $y_c$  channel; the signal has moved to the  $y_s$  channel. The scale factor is now set by the frequency split  $\Delta\omega_o$  rather than the resonator bandwidth  $\beta_y$ . The split frequency effectively sets the bandwidth of the measurement, as indicated by the second order low-pass filter form of the transfer function. In the time domain, the step response is

$$\frac{y_s}{x_a}(t) = \frac{\alpha_z}{\Delta\omega_o} (1 - \cos(\Delta\omega_o t)) \Omega_{zo} u(t), \quad (2.30)$$

where  $\Omega_{zo}$  is the amplitude of the step and  $u(t)$  is the step function. This equation shows the ringing present at the frequency  $\Delta\omega_o$ , limiting the bandwidth of the system to less than this value.

## 2.5 Gyroscope with damping and frequency mismatch

Expanding on the previous section, we now include the effect of damping into the frequency mismatched AM gyroscope. With both effects included, the baseband sense dynamics are

$$\dot{y}_c = -\beta_y y_c + \Delta\omega_o y_s - \alpha_z \Omega_z x_a \quad (2.31)$$

$$\dot{y}_s = -\beta_y y_s - \Delta\omega_o y_c. \quad (2.32)$$

The equations are solved via the Laplace transform. The result is

$$\frac{y_c}{x_a}(s) = -\alpha_z \Omega_z \frac{s + \beta_y}{(s + \beta_y)^2 + \Delta\omega_o^2} \quad (2.33)$$

$$\frac{y_s}{x_a}(s) = \alpha_z \Omega_z \frac{\Delta\omega_o}{(s + \beta_y)^2 + \Delta\omega_o^2}. \quad (2.34)$$

For DC rate inputs, the scale factor for the  $y_c$  and  $y_s$  channels are  $\frac{-\alpha_z \beta_y}{\beta_y^2 + \Delta\omega_o^2}$  and  $\frac{\alpha_z \Delta\omega_o}{\beta_y^2 + \Delta\omega_o^2}$ , respectively.

If  $\beta_y \gg \Delta\omega_o$ , then the signal appears almost entirely in the  $y_c$  channel, in-phase with the drive axis, and the bandwidth is restricted to  $\beta_y$ . The scale factor is approximately  $\frac{-\alpha_z}{\beta_y}$ , a result identical to the analysis in section 2.3. A problem with operating in this regime is that relatively small changes in  $\Delta\omega_o$  will lead to large changes in the scale factor. A typical MEMS gyroscope might have  $\beta_y = 10$  cps. If we assume the modes are initially matched, a 10 cps shift in the split frequency will change the scale factor by 50%. A 10 cps shift is easily possible considering that the natural frequencies of gyroscopes are typically 30 kcps. This would correspond to a 330 ppm relative shift, which could be induced by temperature, stress, shock, or vibration.

If  $\beta_y \ll \Delta\omega_o$ , the signal appears in the  $y_s$  channel, in quadrature with the drive, and the bandwidth is restricted to  $\Delta\omega_o$ . The scale factor is approximately  $\frac{\alpha_z}{\Delta\omega_o}$ , a result identical to the analysis in section 2.4. If  $\Delta\omega_o = 1000$  cps, a 10 cps shift will cause only a 1% variation in the scale factor. Because of the greatly improved scale

factor stability and increased bandwidth, this operating regime is preferred for AM rate gyros.

## 2.6 Gyroscope with cross-axis spring and damper coupling

Cross-axis spring and damper coupling errors are represented by the off-diagonal terms in the  $\mathbf{K}$  and  $\mathbf{C}$  matrices, respectively. This section will examine the impact of these terms on the rate bias error introduced to the frequency-mismatched AM gyroscope.

The full equations (2.8) and (2.9) (excluding force inputs) are used to find the sense axis solutions,

$$\frac{y_c}{x_a}(s) = \frac{(\Omega_c + \alpha_z \Omega_z)(s + \beta_y) - \Omega_{kx} \Delta\omega_o}{(s + \beta_y)^2 + \Delta\omega_o^2} \quad (2.35)$$

$$\frac{y_s}{x_a}(s) = \frac{\Delta\omega_o(\Omega_c + \alpha_z \Omega_z) - \Omega_{kx}(s + \beta_y)}{(s + \beta_y)^2 + \Delta\omega_o^2}. \quad (2.36)$$

In comparison to the previous section, there are now two bias errors introduced. For DC rates with  $\Delta\omega_o \gg \beta_y$ ,

$$\frac{y_c}{x_a}(0) \approx (\Omega_c + \alpha_z \Omega_z) \frac{\beta_y}{\Delta\omega_o^2} - \frac{\Omega_{kx}}{\Delta\omega_o} \quad (2.37)$$

$$\frac{y_s}{x_a}(0) \approx \frac{1}{\Delta\omega_o} (\Omega_c + \alpha_z \Omega_z) - \frac{\Omega_{kx}}{\Delta\omega_o^2} \beta_y. \quad (2.38)$$

The input referred bias error assuming perfect demodulator phase ( $y_s$  recovered perfectly without any contribution from  $y_c$ ) is

$$\Omega_{zbi} = \frac{1}{\alpha_z} \left( \Omega_c - \Omega_k \frac{\beta_y}{\Delta\omega_o} \right). \quad (2.39)$$

The cross-spring bias  $\Omega_k$  is typically much larger than the cross-damper  $\Omega_c$ , with uncompensated values in the range of 10 to 1000 deg/s. The cross-spring bias is rejected substantially with  $\Delta\omega_o \gg \beta_y$ , but this is at the cost of lower sensitivity. Additionally, there is a large error present in the  $y_c$  channel,

$$\Omega_{z bq} = \frac{1}{\alpha_z} \left( \Omega_c \frac{\beta_y}{\Delta\omega_o} - \Omega_k \right) \quad (2.40)$$

known as quadrature error due to being  $90^\circ$  out of phase with the signal. Although the quadrature error is theoretically rejected through a synchronous AM demodulation process, this requires the phase of the rate signal to be known exactly. For example, a  $1^\circ$  with  $100^\circ/\text{s}$  quadrature error is a  $1.7^\circ$  bias error.

The error  $\Omega_{zbi}$  is indistinguishable from rate in this operating mode. This is a dominant source of zero rate output in MEMS gyroscopes.

## 2.7 Noise in the mode-matched AM gyroscope

Equations (2.8) and (2.9) are used to predict the impact of Brownian motion and electronics noise on the white rate noise. The Brownian motion is modeled as force noise by adding  $F_{ycn}$  and  $F_{ysn}$  into  $F_{yc}$  and  $F_{ys}$ , respectively, with power spectral densities  $S_{F_{yc}}(\omega) = S_{F_{ys}}(\omega)$ . The electronics noise effectively corrupts the measurement of the displacement signal from the gyroscope. This noise can be input referred to a displacement noise for each axis denoted  $x_{ae}$ ,  $y_{ce}$ , and  $y_{se}$ .

The noise is first analyzed for the mode-matched case with  $\Delta\omega_o = 0$ . The cross coupling terms  $\Omega_k$  and  $\Omega_c$  are ignored, as their effect is small compared to the direct noise terms. We set  $\Omega_z = 0$  and take a Laplace transform of (2.8) to get

$$y_c = \frac{1}{2m\omega_{ox}} \frac{F_{ys}}{s + \beta_y}. \quad (2.41)$$

Adding in the displacement noise components and considering the response at low frequency only (within the measurement bandwidth), we obtain

$$y_{cn} = \frac{1}{2m\omega_{ox}} \frac{F_{ysn}}{\beta_y} + y_{ce}. \quad (2.42)$$

The noise is input referred to rate noise by multiplying by the inverse of the scale factor found in section 2.3 to give

$$\Omega_n = \frac{1}{\alpha_z} \left( \frac{1}{2m\omega_{ox}x_a} F_{ysn} + \frac{y_{ce}}{x_a} \beta_y \right). \quad (2.43)$$

The PSD of the rate noise is then

$$S_\Omega(\omega) = \frac{1}{\alpha_z^2} \left( \frac{S_{F_{ys}}(\omega)}{4m^2\omega_{ox}^2 x_{rms}^2} + \frac{S_{y_{ce}}(\omega) \beta_y^2}{x_{rms}^2} \right), \quad (2.44)$$

where  $x_{\text{rms}} = x_a/\sqrt{2}$  is the root mean square (RMS) value of the  $x$ -axis displacement. Assuming the force noise is white and contributed entirely by the resonator<sup>2</sup>, we have  $S_{F_{ys}} = 2k_B T c_y / c$ . If the PSD of the  $y$ -displacement noise is  $S_{y_e}(\omega)$ , then  $S_{y_{ce}}(\omega) = \frac{1}{2} S_{y_e}(\omega + \omega_{ox})$ . Using the expression for the peak resonator energy  $E_p = m(x_{\text{rms}}\omega_{ox})^2$ , and making the above substitutions gives

$$S_{\Omega}(\omega) = \frac{1}{\alpha_z^2} \left( \underbrace{\frac{k_B T \beta_y}{c E_p}}_{\text{Brownian}} + \underbrace{\frac{S_{y_e}(\omega + \omega_{ox}) \beta_y^2}{2 x_{\text{rms}}^2}}_{\text{readout}} \right). \quad (2.45)$$

It is important to remember that this is a formula for the baseband equivalent PSD:  $\omega = 0$  corresponds to a DC rate input, which would cause a physical response of the system near the gyroscope's resonant frequency  $\omega_{ox}$ .

Assuming  $S_{y_e}(\omega)$  is white around  $\omega_{ox}$ , the angle random walk is found to be

$$h_0 = S_{\Omega}(0) = \frac{1}{\alpha_z^2} \left( \underbrace{\frac{k_B T \beta_y}{c E_p}}_{\text{Brownian}} + \underbrace{\frac{S_{y_e}(\omega_{ox}) \beta_y^2}{2 x_{\text{rms}}^2}}_{\text{readout}} \right). \quad (2.46)$$

The above expression can be refactored to

$$h_0 = \frac{1}{\alpha_z^2} \frac{k_B T \beta_y}{c E_p} (1 + \gamma_o) \quad (2.47)$$

$$\gamma_o = \frac{1}{2} \beta_y k_x \frac{c S_{y_e}(\omega_{ox})}{k_B T}, \quad (2.48)$$

where  $\gamma_o$  is the excess noise factor due to the electronics. To minimize the angle random walk, the resonator should have low loss (small bandwidth) and large peak energy.

## 2.8 Noise in the mismatched AM gyro

Using a similar approach to the previous section but with the assumption  $\Delta\omega_o \gg \beta_y$ , the expression for the noise in the  $y_s$  channel at low frequency is

$$y_{sn} = \frac{-F_{y_{sn}} \Delta\omega_o - \beta_y F_{y_{cn}}}{2m\omega_{ox} \Delta\omega_o^2} + \left( \frac{\Omega_{kx} \beta_y}{\Delta\omega_o^2} + \frac{\Omega_c}{\Delta\omega_o} \right) x_{an} + y_{se}, \quad (2.49)$$

<sup>2</sup>The sense axis is open-loop; electronics noise does not contribute to the  $y$ -axis force noise.

where  $y_{se}$  is noise added by the  $y$ -axis readout electronics. The cross-coupling and direct damping terms will have a negligible impact on the total noise relative to the penalty introduced by frequency mismatch, so the above can be simplified to

$$y_{sn} = -\frac{F_{ysn}}{2m\omega_{ox}\Delta\omega_o} + y_{se}. \quad (2.50)$$

Multiplying through by the inverse scale factor found in section 2.4, the rate noise is

$$\Omega_n = \frac{1}{\alpha_z} \left( -\frac{F_{ysn}}{2m\omega_{ox}x_a} + \Delta\omega_o \frac{y_{se}}{x_a} \right). \quad (2.51)$$

The PSD of the rate noise is

$$S_\Omega(\omega) = \frac{1}{\alpha_z^2} \left( \frac{S_{F_{ys}}}{4m^2\omega_{ox}^2 x_{rms}^2} + \Delta\omega_o^2 \frac{S_{y_{se}}(\omega)}{x_{rms}^2} \right). \quad (2.52)$$

This expression is identical in form to (2.44), and is simplified in an identical manner to give

$$S_\Omega(\omega) = \frac{1}{\alpha_z^2} \left( \underbrace{\frac{k_B T \beta_y}{c E_p}}_{\text{Brownian}} + \underbrace{\frac{S_{y_e}(\omega + \omega_{ox}) \Delta\omega_o^2}{2x_{rms}^2}}_{\text{readout}} \right). \quad (2.53)$$

Assuming  $S_{y_e}$  is white about  $\omega = 0$ , the angle random walk is

$$h_0 = \frac{1}{\alpha_z^2} \frac{k_B T \beta_y}{c E_p} (1 + \gamma_o) \quad (2.54)$$

$$\gamma_o = \frac{\Delta\omega_o^2 k_x c S_{y_e}(\omega_{ox})}{2\beta_y k_B T}. \quad (2.55)$$

If the electronics noise is dominant, (2.54) is more conveniently expressed as

$$h_0 \approx \frac{\Delta\omega_o^2 S_{y_e}(\omega_{ox})}{2\alpha_z^2 x_{rms}^2}, \quad (2.56)$$

where it is clear that the ratio of the displacement noise PSD to the oscillation amplitude is critical, and the frequency split  $\Delta\omega_o$  acts as a noise penalty. The ratio of noise to oscillation amplitude can equivalently be thought of as a phase noise: it would be the phase noise of a clock with the  $x$ -axis oscillation amplitude and the  $y$ -axis noise.

Comparing the above to (2.47) and (2.48), the contribution from the resonator Brownian noise is the same, but the electronics contribution changes. The noise penalty  $\gamma_r$  from the mode-mismatch is given by the ratio of (2.55) to (2.48) as

$$\gamma_r = \frac{\gamma_{o,\text{mismatch}}}{\gamma_{o,\text{mode-match}}} = \frac{\Delta\omega_o^2}{\beta_y^2}. \quad (2.57)$$

This penalty is very significant, as the mode-mismatched gyro is intentionally designed with  $\Delta\omega_o^2 \gg \beta_y^2$  in order to enable high bandwidth operation and stable scale factor. A typical MEMS gyro may have  $\Delta\omega_o = 1$  kcps and  $\beta_y = 10$  cps, giving  $\gamma_r = 10^4$ . This is a ratio of noise powers, implying that to maintain the same noise level for both the mode-matched and mismatched gyroscopes, the readout circuit of the latter would have to consume  $10^4$  times more power. MEMS gyroscopes typically consume 5 mW per axis. If it was possible to leverage mode-matching, this number could shrink to  $0.5 \mu\text{W}$ , provided no other noise sources and that the dominant power consumption is the front-end analog electronics.

## 2.9 Conclusion

The conventional AM rate gyroscope detects angular rate by measuring small displacements on the sense axis which are introduced by Coriolis coupling from a large-amplitude drive axis. AM gyroscopes are typically operated with large mode splits in order to achieve high bandwidth and stable scale factor. The mode-split reduces the sensitivity of the gyroscope, and as a consequence, low-noise, high-power electronic readout circuitry is necessary to minimize the rate noise. Matching the modes of the gyroscope improves the sensitivity at the cost of bandwidth and scale factor reliability.

The FM gyroscopes presented in the next two chapters do not suffer from these limitations. FM gyroscopes allow for the improved sensitivity of mode-matching without the drawbacks of low bandwidth or unreliable scale factor.

## Chapter 3

# QFM gyroscope

Conventional mode-mismatched open-loop rate mode gyroscopes suffer from low sensitivity, requiring electronics with extremely low noise, and consequent high power, in order to obtain good angle random walk (ARW) performance. Mode matching the gyroscope results in increased sense axis displacement, reducing the impact of the electronics noise at the expense of decreasing the signal bandwidth and increasing the sensitivity to small frequency matching errors and pressure changes. For example, the scale factor of a mode-matched gyroscope with  $\beta = 10$  cps drops by 50% for a 10 cps (330 ppm) mode mismatch. For clarity, this operating mode is referred to as the amplitude modulated (AM) gyroscope below, due to the sense axis amplitude being proportional to rate.

Electrostatic force feedback can be used to reduce the sensitivity of the scale factor to mechanical damping and frequency matching errors but introduces other sensitivities, such as a dependence on the electromechanical coupling factor, which is a function of both the absolute value of the bias voltage and the drive capacitance. Designing mode-matching loops for rate gyroscopes has proven difficult. Ideally, the energy in the sense mode is zero for a zero rate condition, rendering the natural frequency impossible to observe directly. Pilot tones have been used to observe the sense-axis dynamics off-resonance but achieve only limited mode-matching frequency accuracy [13].

The quadrature frequency modulated (QFM) gyroscope [14] overcomes these prob-

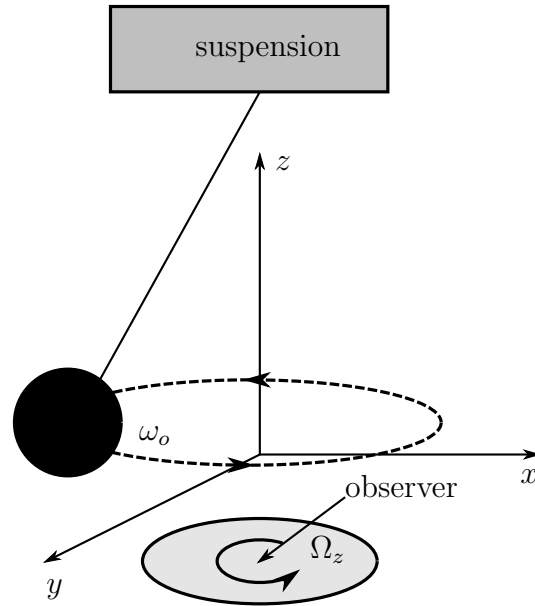


Figure 3.1: QFM gyroscope concept illustrated by Foucault pendulum.

lems by sustaining oscillations in each axis of the gyroscope. Mode-matching is then trivial to achieve, and it will be shown that the QFM scale factor does not depend on the mechanical damping or electromechanical coupling factor.

### 3.1 QFM gyro concept

QFM gyros rely on a nominally symmetric design. Oscillations on the x- and y-axis are controlled to equal amplitude and quadrature phase. The resulting vibration pattern is a circular orbit of the proof mass at a frequency nearly equal to the natural frequency of the sensor, shown in Figure 3.1 for a Foucault pendulum gyroscope.

An outside observer perceives a frequency change of the gyroscope if he rotates relative to the sensor. In a pendulum gyro, the amount of perceived change is equal to the rotation rate, 1 cps per 360 deg/s, independent of temperature, pressure, bias voltages, and fabrication imperfections such as electrode gaps and beam stiffness. The only non-ideality in the scale factor is introduced by the gyroscope's angular gain factor,  $\alpha$ , a value between zero and one which depends on the gyroscope's particular geometry.

### 3.2 Phasor analysis

Similar to the approach used for the AM gyroscope, we use phasor analysis to describe the behavior of the QFM gyroscope. Because the QFM gyroscope is symmetric, it is more convenient to express the solution in terms of the amplitude,  $x_a$ ,  $y_a$ , and phase,  $\phi_x$ ,  $\phi_y$ , of each mode with

$$\mathbf{q}(t) = \begin{bmatrix} x_a(t)e^{j\phi_x(t)} \\ y_a(t)e^{j\phi_y(t)} \end{bmatrix}. \quad (3.1)$$

Differentiating (3.1) and using the assumptions defined in section 2.1 yields

$$\dot{\mathbf{q}}(t) \approx \begin{bmatrix} j\dot{\phi}_x(t)x_a(t)e^{j\phi_x(t)} \\ j\dot{\phi}_y(t)y_a(t)e^{j\phi_y(t)} \end{bmatrix} \quad (3.2)$$

$$\ddot{\mathbf{q}}(t) \approx \begin{bmatrix} e^{j\phi_x(t)} \left( -\dot{\phi}_x^2(t)x_a(t) + j2\dot{\phi}_x(t)\dot{x}_a(t) \right) \\ e^{j\phi_y(t)} \left( -\dot{\phi}_y^2(t)y_a(t) + j2\dot{\phi}_y(t)\dot{y}_a(t) \right) \end{bmatrix}. \quad (3.3)$$

The sustaining forces are defined as

$$\mathbf{F}(t) = \begin{bmatrix} (F_{xc}(t) + jF_{xs}(t)) e^{j\phi_x(t)} \\ (F_{yc}(t) + jF_{ys}(t)) e^{j\phi_y(t)} \end{bmatrix}, \quad (3.4)$$

where  $F_{\{x,y\}c}$  and  $F_{\{x,y\}s}$  are the complex baseband amplitudes of the applied  $x$ - and  $y$ -axis forces with respect to the phase references  $\phi_x$  and  $\phi_y$ . Equations 3.1–3.4 are substituted into (1.1) and simplified to give

$$\dot{x}_a = -\beta_x x_a + \frac{\dot{\phi}_y}{\dot{\phi}_x} (\alpha_z \Omega_z - \Omega_c) y_a \cos \Delta\phi_{xy} + \frac{\Omega_{ky}\omega_{oy}}{\dot{\phi}_x} y_a \sin \Delta\phi_{xy} + \frac{1}{2m\dot{\phi}_x} F_{xs} \quad (3.5)$$

$$\dot{y}_a = -\beta_y y_a - \frac{\dot{\phi}_x}{\dot{\phi}_y} (\alpha_z \Omega_z + \Omega_c) x_a \cos \Delta\phi_{xy} + \frac{\Omega_{kx}\omega_{ox}}{\dot{\phi}_y} x_a \sin \Delta\phi_{xy} + \frac{1}{2m\dot{\phi}_y} F_{ys} \quad (3.6)$$

$$\dot{\phi}_x = \omega_{ox} + (\Omega_c - \alpha_z \Omega_z) \frac{\dot{\phi}_y y_a}{\dot{\phi}_x x_a} \sin \Delta\phi_{xy} + \frac{\Omega_{ky}\omega_{oy}}{\dot{\phi}_x} \frac{y_a}{x_a} \cos \Delta\phi_{xy} - \frac{1}{2m\dot{\phi}_x x_a} F_{xc} \quad (3.7)$$

$$\dot{\phi}_y = \omega_{oy} + (\Omega_c - \alpha_z \Omega_z) \frac{\dot{\phi}_x x_a}{\dot{\phi}_y y_a} \sin \Delta\phi_{xy} + \frac{\Omega_{kx}\omega_{ox}}{\dot{\phi}_y} \frac{x_a}{y_a} \cos \Delta\phi_{xy} - \frac{1}{2m\dot{\phi}_y y_a} F_{yc}, \quad (3.8)$$

where  $\Delta\phi_{xy} = \phi_x - \phi_y$ . The equations have a more natural form if we work with velocity amplitudes rather than displacement. Define  $v_{xa} = \dot{\phi}_x x_a$  and  $v_{ya} = \dot{\phi}_y y_a$ ,

then the equations reduce to

$$\dot{v}_{xa} = -\beta_x v_{xa} + (\alpha_z \Omega_z - \Omega_c) v_{ya} \cos \Delta\phi_{xy} + \Omega_{ky} v_{ya} \sin \Delta\phi_{xy} + \frac{1}{2m} F_{xs} \quad (3.9)$$

$$\dot{v}_{ya} = -\beta_y v_{ya} - (\alpha_z \Omega_z + \Omega_c) v_{xa} \cos \Delta\phi_{xy} + \Omega_{kx} v_{xa} \sin \Delta\phi_{xy} + \frac{1}{2m} F_{ys} \quad (3.10)$$

$$\dot{\phi}_x = \omega_{ox} + (\Omega_c - \alpha_z \Omega_z) \frac{v_{ya}}{v_{xa}} \sin \Delta\phi_{xy} + \Omega_{ky} \frac{v_{ya}}{v_{xa}} \cos \Delta\phi_{xy} - \frac{1}{2m v_{xa}} F_{xc} \quad (3.11)$$

$$\dot{\phi}_y = \omega_{oy} - (\Omega_c + \alpha_z \Omega_z) \frac{v_{xa}}{v_{ya}} \sin \Delta\phi_{xy} + \Omega_{kx} \frac{v_{xa}}{v_{ya}} \cos \Delta\phi_{xy} - \frac{1}{2m v_{ya}} F_{yc}, \quad (3.12)$$

where the approximation  $v_{ia} \approx \omega_{oi} i_a$ ,  $i \in \{x, y\}$  is necessary to make the substitutions in the coefficients of the  $\Omega_{ki}$  terms. This is equivalent to assuming  $|\dot{\phi}_i - \omega_{oi}| \ll \omega_{oi}$ .

The above equations form a system of first order, non-linear ODEs that describe the QFM gyroscope's behavior in the complex baseband. They are useful for demonstrating basic operation, predicting the bias and scale factor, noise analysis, and numerical integration. Note that the AM gyroscope behavior is also captured by the above equations, e.g., the term  $\alpha_z \Omega_z v_{xa} \cos \Delta\phi_{xy}$  in (3.10) represents the Coriolis effect as it applies to the y-axis. However, it is a bit awkward to work with the equations in the above form for AM gyros as the y-axis displacement is typically close to zero, resulting in a poorly defined y-axis phase.

### 3.3 Ideal QFM gyroscope

The ideal QFM gyroscope has  $\mathbf{K} = k\mathbf{I}$  and  $\mathbf{C} = \mathbf{0}$ . Additionally, the gyro is given an initial excitation to start a perfectly circular orbit, so that  $\Delta\phi_{xy} = 90^\circ$  and  $v_{xa} = v_{ya}$ . The sustaining forces are unused, as the system is lossless. The instantaneous frequency equations (3.11) and (3.12) reduce to

$$\dot{\phi}_x = \omega_o - \alpha_z \Omega_z \quad (3.13)$$

$$\dot{\phi}_y = \omega_o - \alpha_z \Omega_z, \quad (3.14)$$

indicating that the instantaneous oscillation frequency is the natural frequency of the device minus the input angular rate. This is the expected behavior as predicted by Figure 3.1.

The inclusion of direct damping terms does not affect the above result. The only requirement is that sustaining amplifiers are put in place to maintain circular oscillation of the proof mass. As long as the oscillators ensure that the velocity amplitudes of the two axes are equal, the scale factor will remain  $-\alpha_z$ .

### 3.4 QFM gyroscope with frequency mismatch

Circular orbits are only possible when the  $x$ - and  $y$ -oscillations are of equal frequency and quadrature phase. The effect of natural frequency mismatch can be compensated by a closed-loop system controlling tuning electrodes (if available). The combination of gyroscope and controller form a phase-locked loop (PLL) with the gyro acting as the voltage-controlled oscillator (VCO). This PLL will ensure both the frequency match and quadrature phase conditions, and the above results for the ideal QFM gyroscope hold.

To analyze the frequency mismatched case, it is convenient to express the instantaneous frequency equations (3.11) and (3.12) as a difference and sum given by

$$\Delta\dot{\phi}_{xy} = \omega_{ox} - \omega_{oy} - \left( \frac{v_{ya}}{v_{xa}} - \frac{v_{xa}}{v_{ya}} \right) \alpha_z \Omega_z \sin \Delta\phi_{xy} \quad (3.15)$$

$$\Sigma\dot{\phi}_{xy} = \omega_{ox} + \omega_{oy} - \left( \frac{v_{ya}}{v_{xa}} + \frac{v_{xa}}{v_{ya}} \right) \alpha_z \Omega_z \sin \Delta\phi_{xy}, \quad (3.16)$$

where the cross-coupling terms are ignored. Direct tuning electrodes enable control of  $\omega_{ox}$  and  $\omega_{oy}$ . The phase difference  $\Delta\phi_{xy}$  is controlled to  $90^\circ$  by adjusting  $\omega_{oy}$  according to (3.15), implying  $\Delta\dot{\phi}_{xy} = 0$ . In this case, the  $y$ -axis phase is slaved to the  $x$ -axis. The reverse is equally valid. Then,  $\omega_{oy} = \omega_{ox}$  and (3.16) reduces to

$$\Sigma\dot{\phi}_{xy} = 2\omega_{ox} - \left( \frac{v_{ya}}{v_{xa}} + \frac{v_{xa}}{v_{ya}} \right) \alpha_z \Omega_z = 2(\omega_{ox} - \alpha_z \Omega_z), \quad (3.17)$$

where the latter expression is valid only when  $v_{xa} = v_{ya}$ .

The above analysis suggests that as long as there is sufficient tuning range, frequency mismatch can be nulled in a closed-loop manner, without the use of pilot-tones or virtual rate signals. This control loop effectively mode-matches the gyroscope. It will be shown that the QFM gyroscope receives the same increased sensitivity benefit from mode-matching as the AM gyroscope.

### 3.5 QFM gyroscope with mechanical cross coupling

Including the cross-coupling effects into (3.11) and (3.12) and assuming  $v_{xa} = v_{ya}$  gives

$$\Delta\dot{\phi}_{xy} = \omega_{ox} - \omega_{oy} + 2\Omega_c \sin \Delta\phi_{xy} \quad (3.18)$$

$$\Sigma\dot{\phi}_{xy} = \omega_{ox} + \omega_{oy} - 2\alpha_z\Omega_z \sin \Delta\phi_{xy} + (\Omega_{kx} + \Omega_{ky}) \cos \Delta\phi_{xy}. \quad (3.19)$$

Similar to the previous analysis, a controller is used to set  $\Delta\phi_{xy} = 90^\circ$ . Due to the anisodamping, we now have  $\omega_{oy} = \omega_{ox} + 2\Omega_c$ . This gives

$$\Sigma\dot{\phi}_{xy} = 2(\omega_{ox} + \Omega_c - \alpha_z\Omega_z), \quad (3.20)$$

which shows that the damper coupling contributes a bias error just as in the case of the AM gyroscope. The quadrature error due to  $\Omega_{ki}$  is rejected as long as the phase difference is held to  $90^\circ$ .

If the frequencies of each axis are controlled differentially, i.e., one frequency is increased and the other decreased, the damper coupling error is rejected. With electrostatic tuning, this is only possible if the tuning electrodes are biased with an offset voltage relative to the proof mass bias. This offset voltage must be extremely stable, as changes in this offset result in changes in the circular orbit frequency. For this reason, it is best to only tune one axis, avoiding the use of parallel plate electrodes for anything else. In this way, the circular orbit frequency is set by the pure mechanical resonant frequency of the master axis, and the gyro bias voltage does not need to be particularly stable or low noise.

### 3.6 Noise in the FM gyroscope

The noise in the QFM gyroscope can be analyzed according the schematic of Figure 3.2. The noise sources  $x_e$  and  $F_{xn}$  model input referred displacement noise of the electronics and brownian force noise due to damping in the mechanical structure,

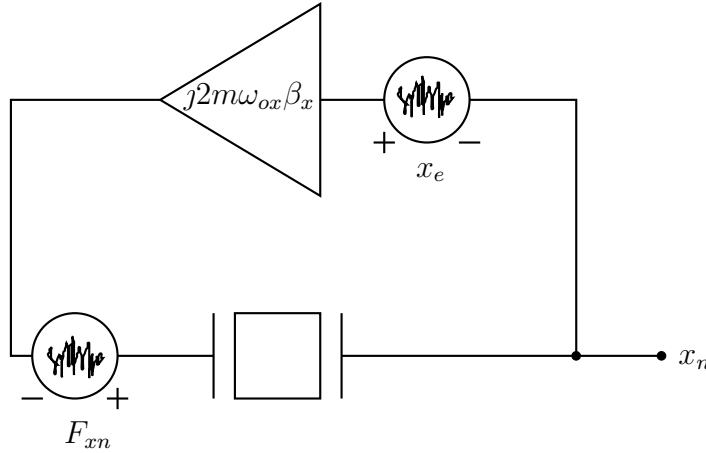


Figure 3.2: Circuit used for evaluating noise of QFM gyroscope.

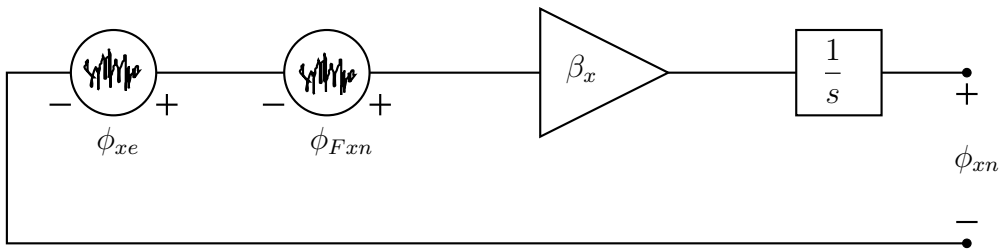


Figure 3.3: Phase domain representation of circuit in Figure 3.2.

respectively. The displacement to force gain of the sustaining amplifier,  $j2m\omega_{ox}\beta_x$ , corresponds to a loop gain of 1. Equivalently, the nominal sustaining force amplitude  $F_{xao}$  necessary to maintain a particular velocity amplitude  $v_{xao} = \omega_{ox}x_{ao}$  is  $F_{xao} = 2m\beta_x v_{xao}$ . The multiplication by  $j$  represents a  $90^\circ$  phase shift which compensates for the phase lag in the force to displacement transfer function of the resonator. The phase lead is often implemented with two  $90^\circ$  phase lags and an inversion as in the Pierce oscillator.

The phasor analysis technique presented in previous sections is ideal for calculating the rate noise. In the absence of rate, anisostiffness, and anisodamping, (3.11) and

(3.12) reduce to

$$\dot{\phi}_x = \omega_{ox} - \frac{1}{2mv_{xa}} F_{xc} = \omega_{ox} - \beta_x \frac{F_{xc}}{F_{xao}} \quad (3.21)$$

$$\dot{\phi}_y = \omega_{oy} - \frac{1}{2mv_{ya}} F_{yc} = \omega_{oy} - \beta_y \frac{F_{yc}}{F_{yao}}. \quad (3.22)$$

This is effectively a phase domain representation of the system presented in Figure 3.2. The quantities  $F_{xc}$  and  $F_{yc}$  represent components of the force which are in-phase with the displacement. Ideally, these forces are zero, but brownian noise from the resonator as well as electronic noise will add this unwanted force component. The force components are normalized by the nominal amplitudes  $F_{xao}$  and  $F_{yao}$ ; therefore, it is convenient to model the added noise as *phase* noise. The fact that the displacement noise is multiplied by the sustaining amplifier gain is inconsequential, as the ratio of noise to signal, or phase noise, is constant.

The phase noise components introduced by the electronics in the  $x$  and  $y$  channels, respectively, are  $\phi_{xe}$  and  $\phi_{ye}$  with power spectral densities  $S_{xe}(\omega)/2/x_{\text{rms}}$  and  $S_{ye}(\omega)/2/y_{\text{rms}}$ . The functions  $S_{xe}(\omega)$  and  $S_{ye}(\omega)$  are the power spectral densities of the displacement noise (contributed by the electronics) in each channel. The phase noise components introduced by the resonator in the  $x$  and  $y$  channels are  $\phi_{F_{xn}}$  and  $\phi_{F_{yn}}$ , respectively, with power spectral densities  $S_{F_{xn}} = 2k_B T c_x / F_{x\text{rms}}^2 / c$  and  $S_{F_{yn}} = 2k_B T c_y / F_{y\text{rms}}^2 / c$ .

The expressions for the frequency noise of the measurement including the above noise sources are

$$\dot{\phi}_{xn} \approx -\beta_x (\phi_{xe} + \phi_{F_{xn}}) \quad (3.23)$$

$$\dot{\phi}_{yn} \approx -\beta_y (\phi_{ye} + \phi_{F_{yn}}). \quad (3.24)$$

The phase-noise model corresponding to these equations is shown in Figure 3.3. The effect of amplitude noise contributed by the  $v_{ia}$  terms is ignored as it is negligible compared to the phase noise.

The white frequency noise spectral densities are found to be

$$S_{\dot{\phi}_{xn}} = \frac{S_{xe}(\omega_o)}{2x_{\text{rms}}^2} \beta_x^2 + \frac{k_B T \beta_x}{c E_{px}} \quad (3.25)$$

$$S_{\dot{\phi}_{yn}} = \frac{S_{ye}(\omega_o)}{2y_{\text{rms}}^2} \beta_y^2 + \frac{k_B T \beta_y}{c E_{py}}, \quad (3.26)$$

where  $E_{px}$  and  $E_{py}$  are the peak resonator energies in the two axes and the electronics displacement noise is assumed to be white around  $\omega = \omega_o$ . Angular rate is measured by summing the two frequencies. For simplicity, we assume  $\beta_x = \beta_y = \beta$ ,  $E_{py} = E_{px}$ ,  $S_{ye} = S_{xe}$ , and  $y_{\text{rms}} = x_{\text{rms}}$ . Summing the frequency PSDs and accounting for the scale factor of the measurement given by (3.16),

$$h_0 = \frac{1}{2\alpha_z^2} \frac{k_B T \beta_x}{c E_{px}} (1 + \gamma_o) \quad (3.27)$$

$$\gamma_o = \frac{1}{2} \beta_x k_x \frac{c S_e(\omega_{ox})}{k_B T}, \quad (3.28)$$

where  $\gamma_o$  is the noise penalty from the electronics. This result is nearly identical to that given for the mode-matched AM rate gyroscope in (2.54). The white rate noise performance of the FM gyroscope is approximately equivalent to the mode-matched AM gyroscope but without the penalties of reduced bandwidth or unreliable scale factor. Because large peak energies are maintained in each axis, it is trivial to directly observe the individual resonant frequencies and tune them to match.

An additional advantage is that the rate signal from each axis adds coherently while the noise terms add incoherently. This gives a factor of 2 improvement in the white rate noise PSD in comparison to (2.54).

A potential disadvantage of the FM gyroscope is the dependence on the natural frequency  $\omega_o$ . The natural frequency contributes an offset to the measurement. Instability of the natural frequency will result in instability in the measured rate. The next section as well as the next chapter present solutions that address this problem.

### 3.7 Dual QFM gyroscope

The QFM gyroscope gives several benefits, including improved sensitivity due to mode-matching, reliable scale factor, and large bandwidth in comparison to con-

ventional AM designs. The drawback is a dependence on the mechanical resonant frequency. If the gyroscope is made from silicon, the temperature coefficient is about 30 ppm/K relative to the mechanical resonant frequency. At 30 kcps, a 1 K temperature shift results in a 0.9 cps shift in bias, or 1.2 million°/hr. This is unacceptable temperature dependence and must be compensated.

The dependence on the natural frequency is largely rejected with the addition of a second gyroscope orbiting in the opposite direction. The direction of the circular orbit is set by choice of a +90° or -90° phase relationship between the axes. The second gyroscope has an equal and opposite scale factor: if the observer rotates in the same direction as the orbit of the first gyroscope, it is in the opposite direction of the second gyroscope. The first gyroscope's circular orbit frequency will appear to decrease, and the second, to increase. Therefore, the two circular orbit frequencies are

$$\Sigma \dot{\phi}_{xy1} = 2\omega_{ox1} - 2\Omega_z \quad (3.29)$$

$$\Sigma \dot{\phi}_{xy2} = 2\omega_{ox2} + 2\Omega_z, \quad (3.30)$$

assuming that the  $y$ -axis phase is slaved to the  $x$ -axis through closed-loop tuning control.

The difference of the above frequencies gives

$$\Sigma \dot{\phi}_{xy1} - \Sigma \dot{\phi}_{xy2} = 2\omega_{ox1} - 2\omega_{ox2} - 4\Omega_z. \quad (3.31)$$

Ideally, the two gyroscopes have equal temperature coefficients and mechanical resonant frequencies, thus the difference perfectly cancels the effect of temperature shift. In general, the temperature coefficients and resonant frequencies will be different. Let  $\delta_1$  and  $\delta_2$  be the relative temperature coefficients of the resonant frequencies of the two gyroscopes. Then  $\omega_{ox1} = \omega_{T0x1} (1 + \delta_1 (T - T_0))$  and  $\omega_{ox2} = \omega_{T0x2} (1 + \delta_2 (T - T_0))$ , where  $T_0$  is the temperature at which  $\omega_{T0x1} = \omega_{ox1}|_{T=T_0}$  and  $\omega_{T0x2} = \omega_{ox2}|_{T=T_0}$  are measured and  $T$  is the ambient temperature. Equation (3.31) then becomes

$$\Sigma \dot{\phi}_{xy1} - \Sigma \dot{\phi}_{xy2} = \omega_{T0x1} - \omega_{T0x2} + (\omega_{T0x1}\delta_1 - \omega_{T0x2}\delta_2) \Delta T - 4\Omega_z, \quad (3.32)$$

where  $\Delta T = T - T_0$ . If the temperature coefficients are equal, then the temperature dependence is reduced by the factor  $\omega_{T0x}/(2(\omega_{T0x1} - \omega_{T0x2}))$ , which gives several

orders of magnitude improvement. For example, with a 100 cps frequency mismatch between the two gyros and 30 kcps natural frequency, the temperature dependence is reduced by a factor of 60,000. This would result in less than  $20^\circ/\text{hr}$  bias for 1 K temperature shift.

### 3.8 Experimental Results

The sensor, fabricated in the Invensense Nasiri Fabrication process [15], consists of two mechanically independent 1 mm, 71 kcps rings integrated with CMOS read-out electronics on a  $2.9 \times 2.4 \text{ mm}^2$  die. Figure 3.5 shows a picture of one of the ring gyroscopes. The ring is 1 mm in diameter and  $6 \mu\text{m}$  wide. The resonant frequency is about  $\omega_o = 71 \text{ kcps}$  and the resonator bandwidth in 1 mTorr vacuum is about  $\beta = 0.4 \text{ cps}$ . The mechanical angle random walk is found from (3.28) as  $h_{om} = (3.9 \text{ mdps}/\sqrt{\text{cps}})^2$ .

Figure 3.4 shows the CMOS layout. The integrated electronics allow a dense array of 96 separate electrodes for drive, sense, frequency tuning, and quadrature null. The electrodes are arranged in differential pairs across the ring. Table 3.1 gives the functionality of all electrode pairs. The sense and drive electrodes are offset by one another by  $15^\circ$ . This effect is compensated by an electronic rotation of the drive voltages of the gyroscope. The tuning electrodes are also rotated with respect to the orthogonal modes of the gyroscope. Again, pre-multiplication of the tuning signals by a rotation matrix corrects the offset.

To minimize parasitics, capacitive sensing is conducted using 12 separate pseudo-differential buffer amplifiers within each ring structure—Figure 3.6. The capacitance of a single pick-off is 6 fF. Integrated electronics achieve  $S_e = (32 \text{ fm}/\sqrt{\text{cps}})^2$  displacement noise density, resulting in  $\gamma_o = 50 \text{ ppm}$ , thus the noise from the buffer amplifiers should be negligible.

The ring gyroscopes operate in the 3-theta flexural mode, where the x- and y-modes are  $30^\circ$  apart. In conventional AM gyroscopes, a standing wave pattern is formed on the drive-axis and the Coriolis force is read out by electrodes located at the antinodes of the sense-mode. In QFM operation, there is no longer a standing wave

Function	Electrode pairs [°]
Sense 1	0, 60, ..., 300
Sense 2	30, 90, ..., 330
Drive 1	15, 75, ..., 315
Drive 2	45, 105, ..., 345
Tune 1	7.5, 67.5, ..., 307.5
Tune 2	37.5, 97.5, ..., 337.5
Tune 3	22.5, 82.5, ..., 322.5
Tune 4	52.5, 112.5, ..., 352.5

Table 3.1: Ring gyroscope electrode functionality.

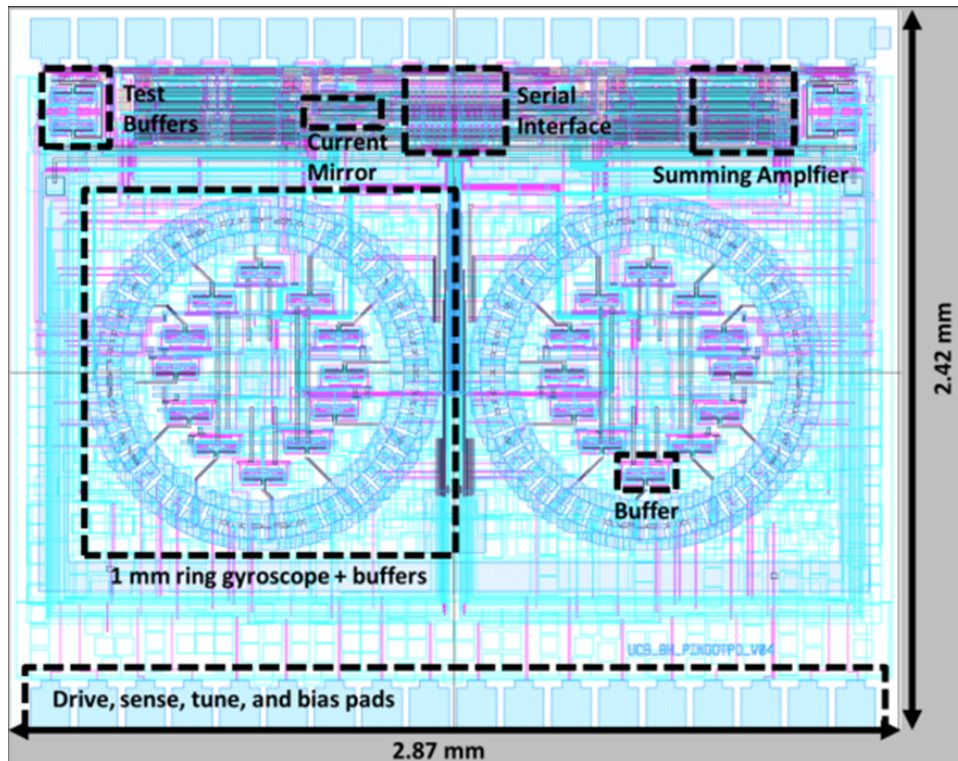


Figure 3.4: Layout diagram of ring gyroscope test-chip.

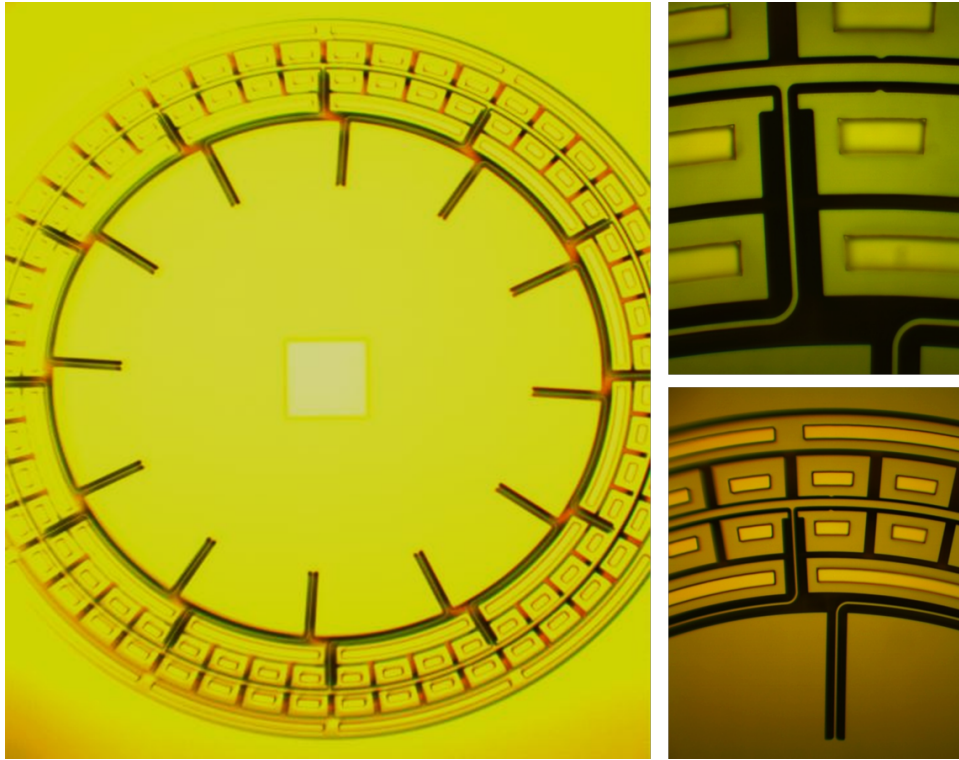


Figure 3.5: Photograph of ring gyroscope device.

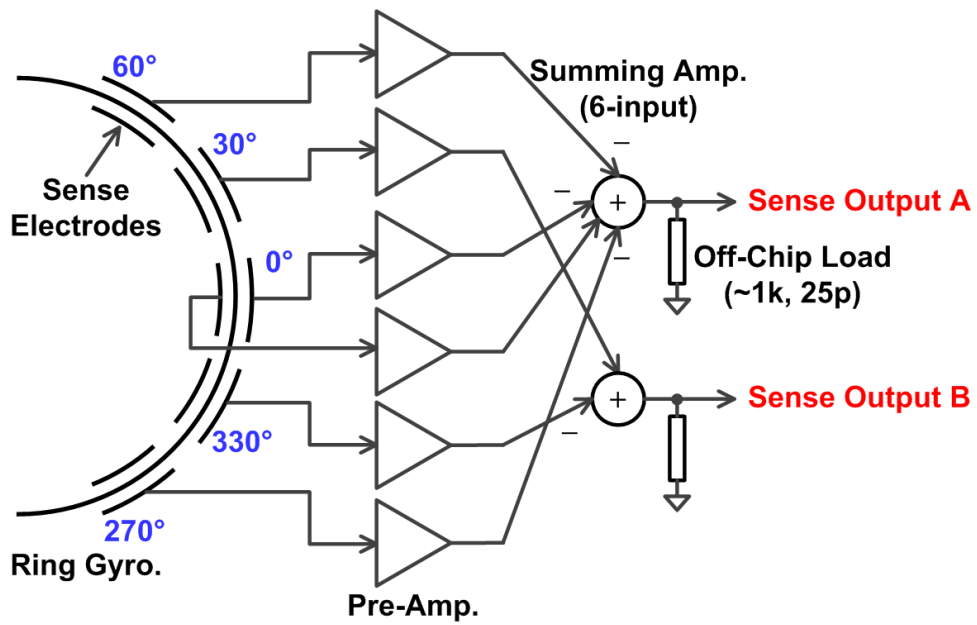


Figure 3.6: Partial schematic of ring gyroscope electrode connections.

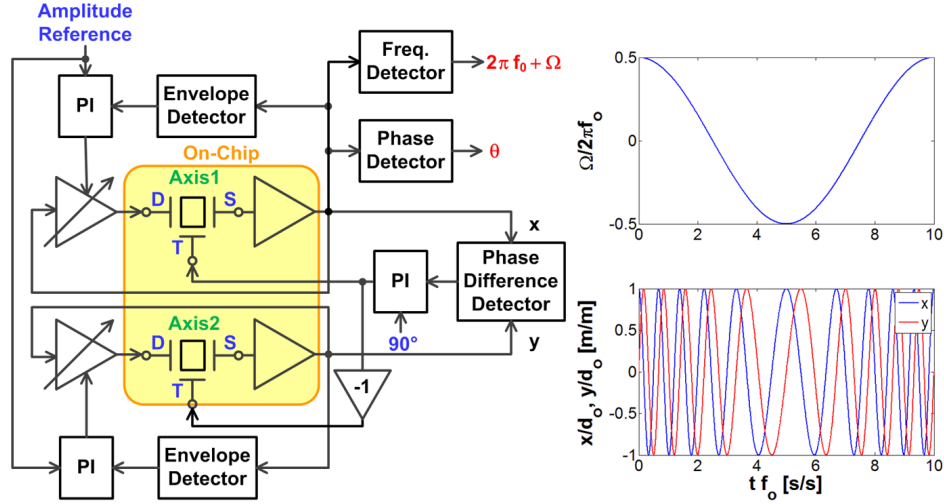


Figure 3.7: The QFM controller maintains equal velocity amplitude oscillations on each axis and additionally mode-matches the gyroscope.

with fixed nodes and anti-nodes. Instead, the nodes and anti-nodes move together along the circumference of the ring at an angular rate close to the natural frequency of the gyroscope. The results derived in the previous sections also apply to ring and hemisphere gyroscopes with adjustments to angular slip factor  $\alpha_z$  and modal mass  $m$ . In the 3-theta ring gyroscope,  $\alpha_z = 0.6$  and  $m \approx (5/9)m_{\text{ring}} = 0.8 \mu\text{g}$ , where  $m_{\text{ring}}$  is the mass of the ring.

Figure 3.7 shows the controller architecture for maintaining a circular orbit. The  $x$ - and  $y$ -displacements are in quadrature and of equal amplitude. The controller was implemented with analog electronics on a PCB. The oscillator consists of a differentiator, variable gain amplifier, envelope detector and PI controller. The relative phase of the oscillations is detected through analog multiplication of the two displacement signals, and an additional PI controller adjusts the tuning voltage of one axis in order to hold the phase shift to  $90^\circ$ . The displacement signals are digitized by 12-bit, 100 MS/s ADCs, and the FM demodulation is done in software.

Figure 3.8 shows the measured Allan deviation. The bias stabilities of the single and dual mass gyros are  $1550$  and  $370^\circ/\text{hr}$  at  $0.3$  and  $8.2$  s averaging time, respectively. The single mass gyro tests were performed in a  $25 \pm 0.1^\circ\text{C}$  temperature controlled environment; the temperature was not regulated for the dual mass test. At  $8.2$  s, the

dual mass gyro achieves an order-of-magnitude better performance than the single mass design. The white rate noise is 0.13 and 0.09 deg/s/rt-Hz, respectively. The rate noise is much more than predicted by the mechanical and buffer amplifier contributions. The additional noise is due to a combination of effects: supply noise and quantization noise of the ADCs.

The QFM mode is sensitive to noise on the bias supply when parallel plate drive and sense electrodes are used due to the spring-softening effect. The noise density of the bias supply is multiplied by the voltage to frequency gain of the parallel plate electrode and appears directly as noise and drift of the measured frequency. The ADC quantization noise effectively adds white phase noise to the displacement signal before the FM demodulation. As an example, sub-10 mdps/ $\sqrt{\text{cps}}$  noise density at a 100 cps offset from the carrier requires better than -140 dBc noise in a 1 cps bandwidth. This suggests that direct digitization of the sine wave is impractical, and that specialized frequency-to-digital converters are required. The solution presented in the next chapter addressed these issues.

### 3.9 Conclusion

Compared to the AM gyroscope, the QFM gyro has advantages of high sensitivity due to mode-matching, unrestricted bandwidth, and reliable scale factor, but has the disadvantage of bias dependence on resonant frequency.

The QFM gyroscope is well-suited to high bandwidth or AC coupled applications where increased bias drift (mainly due to temperature effects on the Young's modulus) are acceptable. These applications include gaming, image stabilization, and gesture recognition. In this situation, a large power savings in the electronics is possible due to the benefit of mode-matching.

Experimental results prove the concept of the QFM operating mode. The scale factor is confirmed to be equal to the angular gain factor of the gyroscope. Addition of a second gyroscope greatly improves the bias stability, but frequency tracking between the two resonators must be better than parts-per-billion. The two rings were demonstrated to track one another within 6 ppb, corresponding to 370 °/hr at 71 keps

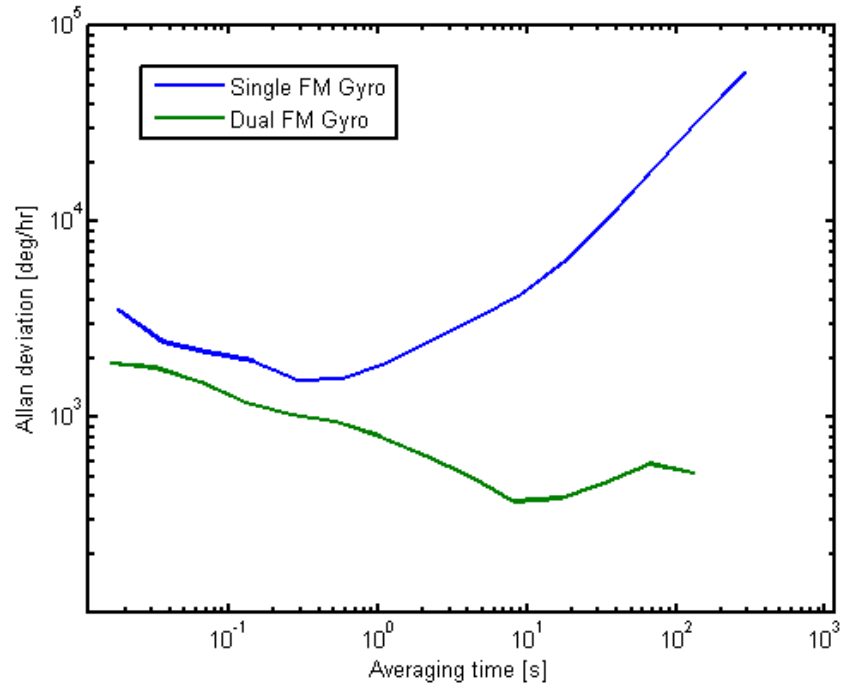


Figure 3.8: Allan deviation comparison between single and dual QFM gyroscopes.

resonant frequency, which would be a little better than  $10^\circ/\text{hr}$  with a 1 kcps resonant frequency.

The next chapter describes a technique that can be used in combination with both AM and FM gyroscopes to reject bias errors due to anisodamping and resonant frequency drift. This enables FM gyroscopes to be used in applications where low bias-drift is a requirement.

## Chapter 4

# Lissajous pattern gyroscope

In the previous chapter, the QFM gyroscope was described and motivated. The QFM gyroscope has the unique property that the modes can be matched while preserving bandwidth and scale factor stability. The disadvantage is that any changes to the resonant frequency appear as rate instability. We proposed to use two structures with proof masses orbiting in opposite directions in order to cancel changes in the resonant frequency due to temperature. Here, we present an alternative method that relies on modulating the rate sensitivity of the FM gyroscope between -1 and 1.

Conceptually, we can change the sign of the rate sensitivity by changing the direction of the circular orbit. This is confirmed by our phase-domain model of the FM gyroscope. From (3.16) with  $v_{xa} = v_{ya}$  and ignoring cross-axis damping, we find

$$\Sigma \dot{\phi}_{xy} = \omega_{ox} + \omega_{oy} - 2\alpha_z \Omega_z \sin \Delta\phi_{xy}. \quad (4.1)$$

If  $\Delta\phi_{xy} = 90^\circ$ , x leads y, thus the orbit is counter-clockwise, and  $\sin \Delta\phi_{xy} = 1$ . If  $\Delta\phi_{xy} = -90^\circ$ , y leads x; the orbit is clockwise; and  $\sin \Delta\phi_{xy} = -1$ . By switching  $\Delta\phi_{xy}$  between these two states, the rate signal is amplitude modulated to a higher frequency. The AM carrier in this case is determined by the rate that we switch between the two states.

The concept of orbital direction switching is to the QFM gyroscope as mode-reversal is to the AM gyroscope. In mode-reversal, the drive and sense axis are periodically swapped in order to cancel errors due to asymmetry [16, 17]. Reversing

the modes of the gyroscope requires continuously ringing up and down the drive and sense axes. The rate of the mode-reversal is limited by the start-up time of the drive oscillator. Because of this constraint, typical mode-reversal rates are on the order of 1 Hz or less. This limits the bandwidth of the measurement and the amount of attenuation of low frequency errors.

In order to increase the mode-reversal rate, an alternative strategy is to continuously transition between the states, without ever intentionally removing energy from the gyroscope. This is possible if both axes are continuously excited, and only the phase relationship between the two vibrations is controlled.

For example, suppose the gyroscope is initially vibrating along a  $45^\circ$  angle. The individual x- and y- vibrations are then equal in amplitude and in-phase with one another. The sense axis is along along a  $135^\circ$  angle. In order to implement mode-reversal, we must transition the gyroscope so that the drive axis is along  $135^\circ$  and the sense axis is along  $45^\circ$ . The conventional way to do this is to ring down the current drive axis, then ring up the new drive axis, which takes a very long time. A fast way to do this is to simply change the phase relationship between the x- and y-axes from  $0^\circ$  to  $180^\circ$ . If tuning electrodes are available, this is easily accomplished with a phase-locked loop. The y-axis frequency is temporarily increased to create the desired phase shift, and then decreased to again match the x-axis. The same strategy is employed for orbital direction switching by switching the phase shift between  $90^\circ$  and  $-90^\circ$ . The rate of switching is limited only by the tuning range of the gyroscope. For example, if the range is only 1 cps, this limits the amount of phase shift that can be created in 1 s to  $360^\circ$ . This means that it would take at least half of a second to switch the direction of the orbit. Fortunately, it is easily possible to have hundreds of cps of tuning range, so the direction switching can be as fast as single milliseconds.

An alternative approach to implementing mode-reversal or orbital direction switching is to simply let each oscillator run at the natural frequency of the axis. Two sinusoidal oscillators at different frequencies form a Lissajous pattern when their trajectory is plotted on an x-y graph—Figure 4.1. Because of this, we refer to these operating modes as Lissajous FM (LFM) and Lissajous AM (LAM).

The Lissajous pattern can be thought of as a progression of continuous states. The

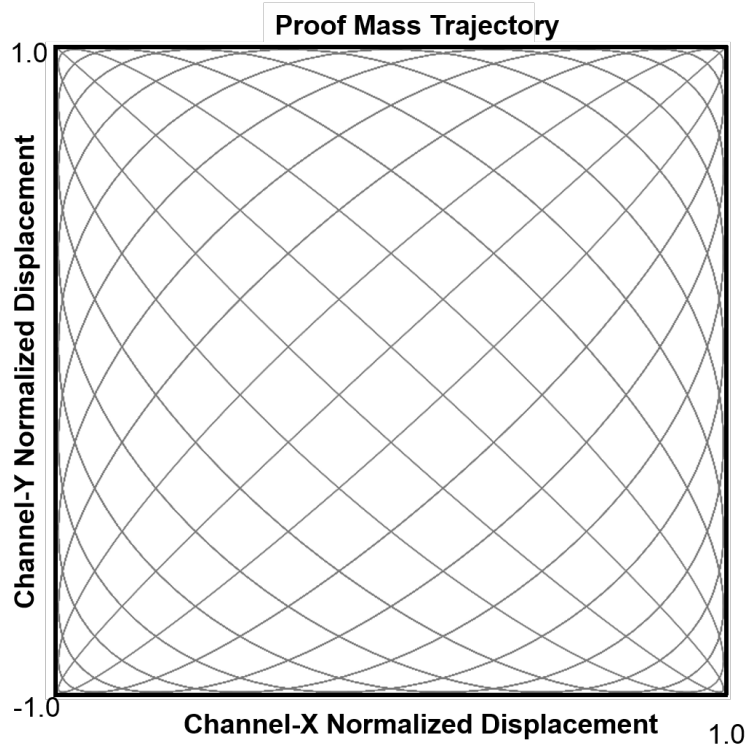


Figure 4.1: The trajectory of the proof mass when the x- and y-axis oscillators run at different frequencies creates a Lissajous pattern.

phase shift between the oscillations will continuously increase as a ramp function. A few interesting points along this ramp are phase differences of (1) 0, (2) 90, (3) 180, and (4) 270 degrees. At these specific instances in time, the proof mass trajectory will be (1) a straight line at a 45 degree angle, (2) counter-clockwise circular orbit, (3) a straight line at a 135 degree angle, and (4) a clockwise orbit. This pattern will repeat with a frequency equal to the difference frequency between the oscillations. For FM readout, the rate sensitivity in each state is (1) 0, (2) -1, (3) 0, and (4) 1. Because the Lissajous pattern gives a continuous transition between these four states, we will find that the sensitivity varies sinusoidally as a function of the phase difference.

## 4.1 Ideal LFM gyroscope

In the absence of mechanical cross coupling, the instantaneous frequency equations (3.11) and (3.12) reduce to

$$\dot{\phi}_x = \omega_{ox} - \alpha_z \frac{v_{ya}}{v_{xa}} \Omega_z \sin \Delta\phi_{xy} \quad (4.2)$$

$$\dot{\phi}_y = \omega_{oy} - \alpha_z \frac{v_{xa}}{v_{ya}} \Omega_z \sin \Delta\phi_{xy}. \quad (4.3)$$

We assume that the natural frequencies of the LFM gyroscope are mismatched. If they are not mismatched, a frequency split can be introduced by tuning the gyroscope axes. In the case of perfectly matched natural frequencies, the operation reduces to the QFM gyroscope of Chapter 3. In this sense, the LFM gyroscope is a more general concept of the QFM gyroscope, but we treat them separately here due to their very different design trade-offs.

It is convenient to express (4.2) and (4.3) as a difference and sum given by

$$\Delta\dot{\phi}_{xy} = \omega_{ox} - \omega_{oy} - \left( \frac{v_{ya}}{v_{xa}} - \frac{v_{xa}}{v_{ya}} \right) \alpha_z \Omega_z \sin \Delta\phi_{xy} \quad (4.4)$$

$$\Sigma\dot{\phi}_{xy} = \omega_{ox} + \omega_{oy} - \left( \frac{v_{ya}}{v_{xa}} + \frac{v_{xa}}{v_{ya}} \right) \alpha_z \Omega_z \sin \Delta\phi_{xy}. \quad (4.5)$$

Equation (4.4) is a first-order nonlinear differential equation with the exact solution

$$\tan \left( \frac{1}{2} \Delta\phi_{xy} \right) = \frac{\sqrt{(\omega_{ox} - \omega_{oy})^2 - (\Delta r_v \alpha_z \Omega_z)^2} \tan \left( \frac{1}{2} \sqrt{(\omega_{ox} - \omega_{oy})^2 - (\Delta r_v \alpha_z \Omega_z)^2} t \right)}{\omega_{ox} - \omega_{oy}} + \frac{\Delta r_v \alpha_z \Omega_z}{\omega_{ox} - \omega_{oy}}, \quad (4.6)$$

where  $\Delta r_v = \frac{v_{ya}}{v_{xa}} - \frac{v_{xa}}{v_{ya}}$  and  $\Delta\phi_{xy}(0) = 0$ . In the preferred operation,  $v_{xa} \approx v_{ya}$  thus  $\Delta r_v \alpha_z \Omega_z \ll \omega_{ox} - \omega_{oy}$ , and the solution can be simplified to

$$\Delta\phi_{xy} \approx (\omega_{ox} - \omega_{oy}) t. \quad (4.7)$$

The expression for the frequency sum then becomes

$$\Sigma\dot{\phi}_{xy} = \omega_{ox} + \omega_{oy} - \left( \frac{v_{ya}}{v_{xa}} + \frac{v_{xa}}{v_{ya}} \right) \alpha_z \Omega_z \sin (\omega_{ox} - \omega_{oy}) t. \quad (4.8)$$

The rate signal is modulated to the frequency  $\omega_{ox} - \omega_{oy}$  (typically 100 cps) while the offset  $\omega_{ox} + \omega_{oy}$  (typically 60 kcps) is not. This allows the rate signal to be separated from the drift of the resonant frequency.

The LFM readout algorithm is then:

1. Drive both axes into self-oscillation at their natural frequencies. These frequencies can optionally be adjusted via tuning electrodes to achieve the desired frequency split.
2. Measure the sum of the two frequencies  $\Sigma \dot{\phi}_{xy}$ . Optionally high pass filter this quantity to remove the natural frequency component.
3. Measure the phase difference between the two oscillations  $\Delta \phi_{xy}$ .
4. Multiply  $\Sigma \dot{\phi}_{xy}$  by  $\sin \Delta \phi_{xy}$ .
5. Low-pass filter the result to remove the DC feed-through and image components at frequencies  $\Delta \dot{\phi}_{xy}$  and  $2\Delta \dot{\phi}_{xy}$ .

Following these steps, the result is

$$\left( h_{HP} * \Sigma \dot{\phi}_{xy} \right) (t) \approx -\frac{1}{2} \left( \frac{v_{ya}}{v_{xa}} + \frac{v_{xa}}{v_{ya}} \right) \alpha_z \Omega_z(t) \sin \Delta \phi_{xy}(t) \quad (4.9)$$

$$\left( h_{HP} * \Sigma \dot{\phi}_{xy} \right) (t) \sin \Delta \phi_{xy}(t) \approx \quad (4.10)$$

$$-\frac{1}{2} \left( \frac{v_{ya}}{v_{xa}} + \frac{v_{xa}}{v_{ya}} \right) \alpha_z \Omega_z(t) (1 - \cos(2\Delta \phi_{xy}(t)))$$

$$\left( h_{LP} * \left( \left( h_{HP} * \Sigma \dot{\phi}_{xy} \right) \sin \Delta \phi_{xy} \right) \right) (t) \approx -\frac{1}{2} \left( \frac{v_{ya}}{v_{xa}} + \frac{v_{xa}}{v_{ya}} \right) \alpha_z \Omega_z(t), \quad (4.11)$$

where  $h_{HP}(t)$  and  $h_{LP}(t)$  are the impulse responses of the high-pass and low-pass filters. The high pass filter is assumed to be a DC block filter, and the low-pass filter is assumed to be a brick-wall filter with bandwidth  $|\omega_{ox} - \omega_{oy}|$ . The final result only holds when the bandwidth of the input rate signal  $\Omega_z(t)$  is restricted to  $|\omega_{ox} - \omega_{oy}|$ . Otherwise, aliasing of the signal will occur. This imposes a bandwidth dependence on the split frequency. Practical designs should have the split frequency much greater than the desired rate bandwidth.

The scale factor of the measurement is dependent on the quantity  $\Sigma r_v = \frac{v_{ya}}{v_{xa}} + \frac{v_{xa}}{v_{ya}}$ . Ideally, the velocity amplitudes of the two oscillations are equal, and the total scale factor is simply  $-\alpha_z$ . One interesting property about the sum of ratios that are inverses of one another is that it is insensitive to small changes in either quantity. The two dimensional Taylor series about  $v_{xa} = v_{ya} = v_a$  is given by

$$\Sigma r_v = \frac{v_{ya}}{v_{xa}} + \frac{v_{xa}}{v_{ya}} \approx 2 + \left(\frac{\Delta v_{xa}}{v_a}\right)^2 + \left(\frac{\Delta v_{ya}}{v_a}\right)^2 - \frac{2\Delta v_{xa}\Delta v_{ya}}{v_a^2}, \quad (4.12)$$

where  $\Delta v_{xa} = v_{xa} - v_a$  and  $\Delta v_{ya} = v_{ya} - v_a$ . There is no linear dependence on the deviation of the velocity from the nominal value. If the deviation changes by 1% relative to the nominal value, there is only a 0.01% variation in the quantity  $\left(\frac{\Delta v_{xa}}{v_a}\right)^2$ . The overall scale factor of the measurement is approximately

$$\alpha_{LFM} \approx -\alpha_z \left(1 + \frac{1}{2} \left(\frac{\Delta v_{xa}}{v_a}\right)^2 + \frac{1}{2} \left(\frac{\Delta v_{ya}}{v_a}\right)^2 - \frac{\Delta v_{xa}\Delta v_{ya}}{v_a^2}\right) \approx -\alpha_z. \quad (4.13)$$

## 4.2 LFM gyroscope with mechanical cross coupling

The difference and sum of the x- and y-axis frequencies are found from (3.11) and (3.12) as

$$\Delta \dot{\phi}_{xy} = \omega_{ox} - \omega_{oy} + (\Sigma r_v \Omega_c - \Delta r_v \alpha_z \Omega_z) \sin \Delta \phi_{xy} + \Delta r_v \Omega_k \cos \Delta \phi_{xy} \quad (4.14)$$

$$\Sigma \dot{\phi}_{xy} = \omega_{ox} + \omega_{oy} + (\Delta r_v \Omega_c - \Sigma r_v \alpha_z \Omega_z) \sin \Delta \phi_{xy} + \Sigma r_v \Omega_k \cos \Delta \phi_{xy}, \quad (4.15)$$

where we assume  $\Omega_k = \Omega_{kx} = \Omega_{ky}$ . If the velocities are constant and closely matched, i.e,  $\Delta r_v \approx 0$ ,  $\Sigma r_v \approx 2$ , and the cross damping error is small compared to the frequency split,  $\Sigma r_v \Omega_c \ll \omega_{ox} - \omega_{oy}$ , the phase difference is approximately

$$\Delta \phi_{xy} = (\omega_{ox} - \omega_{oy}) t. \quad (4.16)$$

The sum of the frequencies is

$$\Sigma \dot{\phi}_{xy} = \omega_{ox} + \omega_{oy} - 2\alpha_z \Omega_z \sin \Delta \phi_{xy} + 2\Omega_k \cos \Delta \phi_{xy}. \quad (4.17)$$

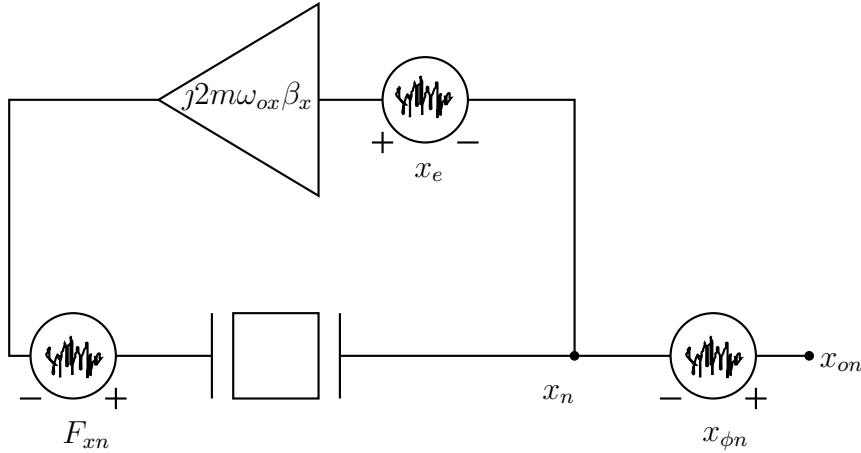


Figure 4.2: Circuit used for evaluating noise of LFM gyroscope.

The rate is found by multiplying the sum of the frequencies by  $\sin \Delta\phi_{xy}$ . To first order, this is a bias-free estimate of the rate. Neither the cross-damper  $\Omega_c$  or cross-spring  $\Omega_k$  errors impact the zero rate output. This is unlike the AM gyroscope, which only attenuates the error  $\Omega_k$  by the factor  $\beta_x/\Delta\omega_o$  and does nothing to the error  $\Omega_c$ . Additionally, the direct damping terms do not affect the FM gyroscope because both axes have closed loop amplitude control.

This implies that LFM gyroscopes can be operated with mode-splits much lower than typically found in AM gyroscope designs. Because the power required by the front-end electronics is proportional to  $\Delta\omega_o^2/\beta^2$ , this can lead to large power savings in the LFM mode, everything else being equal. The LFM mode also gives improved scale factor stability. The scale factor is only affected by the factor  $\alpha_z$  to first order.

### 4.3 Noise in the LFM gyroscope

The noise analysis for the LFM gyroscope very closely follows that for the QFM gyroscope. The circuit of Figure 4.2 shows a single axis of the LFM gyroscope with all relevant noise sources included. In addition to the input referred oscillator noise  $x_e$  and the Brownian force noise  $F_{xn}$ , an extra phase noise source  $x_{\phi n}$  is also considered. This noise source is important to consider in the LFM gyroscope white rate noise

determination.

In chapter 3, the frequency noise at point  $x_n$  in Figure 4.2 was found to be

$$\dot{\phi}_{xn} \approx -\beta_x (\phi_{xe} + \phi_{F_{xn}}). \quad (4.18)$$

The y-axis noise circuit is identical, thus the frequency noise is

$$\dot{\phi}_{yn} \approx -\beta_y (\phi_{ye} + \phi_{F_{yn}}). \quad (4.19)$$

Including the effects of the phase noise generator  $x_{\phi n}$ , the phase noise at points  $x_{on}$  and  $y_{on}$  is

$$\dot{\phi}_{xon} \approx -\beta_x (\phi_{xe} + \phi_{F_{xn}}) + \dot{\phi}_{x\phi n} \quad (4.20)$$

$$\dot{\phi}_{yon} \approx -\beta_y (\phi_{ye} + \phi_{F_{yn}}) + \dot{\phi}_{y\phi n}. \quad (4.21)$$

The PSD of the frequency noise is then

$$S_{\dot{\phi}_{xn}}(\omega) = \frac{S_{xe}(\omega_{ox})}{2x_{\text{rms}}^2} \beta_x^2 + \frac{k_B T \beta_x}{c E_{px}} + S_{\dot{\phi}_{x\phi n}}(\omega) \quad (4.22)$$

$$S_{\dot{\phi}_{yn}}(\omega) = \frac{S_{ye}(\omega_{oy})}{2y_{\text{rms}}^2} \beta_y^2 + \frac{k_B T \beta_y}{c E_{py}} + S_{\dot{\phi}_{y\phi n}}(\omega), \quad (4.23)$$

where  $S_{xe}$ ,  $S_{ye}$ ,  $E_{px}$ , and  $E_{py}$  follow their definitions given in chapter 3. The frequency noise  $S_{\dot{\phi}_{x\phi n}}$  is the only change from the result derived there. The added frequency noise term is due to added electronic noise outside of the oscillator loop. The noise added is predominantly white *phase* noise. This white phase noise must be differentiated to be modeled as frequency noise, giving

$$S_{\dot{\phi}_{x\phi n}}(\omega) = \omega^2 S_{\phi_{x\phi n}} = \frac{1}{2} \frac{\omega^2 S_{x\phi n}}{x_{\text{rms}}^2} \quad (4.24)$$

$$S_{\dot{\phi}_{y\phi n}}(\omega) = \omega^2 S_{\phi_{y\phi n}} = \frac{1}{2} \frac{\omega^2 S_{y\phi n}}{y_{\text{rms}}^2} \quad (4.25)$$

Once again, the frequency  $\omega$  is relative to the gyroscope oscillation frequency. In the LFM gyroscope, we are concerned with the noise at an offset  $\omega_{ox} - \omega_{oy}$  from the carrier. This corresponds to  $\omega = \omega_{ox} - \omega_{oy}$ . Substituting in for  $S_{\dot{\phi}_{x\phi n}}(\omega)$  and factoring the result, we obtain

$$h_0 = \frac{1}{2\alpha_z^2} \frac{k_B T \beta_x}{c E_{px}} (1 + \gamma_o) \quad (4.26)$$

$$\gamma_o = \frac{1}{2} \frac{cm\beta_x\omega_{ox}^2}{k_B T} \left( S_{xe}(\omega_{ox}) + \frac{\Delta\omega_o^2}{\beta_x^2} S_{x\phi n}(\omega_{ox}) \right), \quad (4.27)$$

where  $\Delta\omega_o = \omega_{ox} - \omega_{oy}$ ,<sup>1</sup> and we assume  $\beta_y = \beta_x$ ,  $E_{py} = E_{px}$ ,  $y_{rms} = x_{rms}$ ,  $S_{ye}(\omega_{oy}) = S_{xe}(\omega_{ox})$ , and  $S_{x\phi_n}(\omega_{oy}) = S_{y\phi_n}(\omega_{ox})$ . This result indicates the critical impact of the noise source  $x_{\phi_n}$ . The noise power contribution increases with the square of the difference frequency! In order for the noise contributions of the two electronic noise sources to be equal, the one outside the loop must dissipate on the order of  $\Delta\omega_o^2/\beta_x^2$  more power. This result is almost identical to the noise penalty derived for the mismatched AM gyroscope.

## 4.4 AM readout of Lissajous gyroscope

In the LFM gyroscope, the rate information is contained in not only the frequencies of the oscillations, but also in the displacements or applied forcing voltages used to maintain the Lissajous figure. Amplitude readout generally will have a less reliable scale factor than frequency readout and is extremely sensitive to non-linearity in the signal path, but it is possible if high resolution frequency measurement is unavailable.

Equations (3.9) and (3.10) show the relationship between velocity amplitudes, applied forces, and input rate. With sustaining amplifiers providing forces compensating for the resonator damping, the velocity amplitudes of the axes, assuming  $|\alpha_z\Omega_z| + |\Omega_c| \ll |\Delta\omega_o|$ , are

$$\begin{aligned} v_{xa} &\approx \int (\alpha_z\Omega_z - \Omega_c) v_{yao} \cos \Delta\phi_{xy} dt + \int \Omega_{ky} v_{yao} \sin \Delta\phi_{xy} dt + v_{xao} \\ &= \frac{\alpha_z\Omega_z - \Omega_c}{\Delta\dot{\phi}_{xy}} v_{yao} \sin \Delta\phi_{xy} - \frac{\Omega_{ky}}{\Delta\dot{\phi}_{xy}} v_{yao} \cos \Delta\phi_{xy} + v_{xao} \end{aligned} \quad (4.28)$$

$$\begin{aligned} v_{ya} &\approx \int (-\alpha_z\Omega_z - \Omega_c) v_{xao} \cos \Delta\phi_{xy} dt + \int \Omega_{kx} v_{xao} \sin \Delta\phi_{xy} dt + v_{yao} \\ &= \frac{-\alpha_z\Omega_z - \Omega_c}{\Delta\dot{\phi}_{xy}} v_{xao} \sin \Delta\phi_{xy} - \frac{\Omega_{kx}}{\Delta\dot{\phi}_{xy}} v_{xao} \cos \Delta\phi_{xy} + v_{yao}. \end{aligned} \quad (4.29)$$

The subtraction of the two velocities cancels the damper coupling term. The rate signal is modulated to the split frequency  $\Delta\omega_o$ .

Measurement of the rate requires two AM demodulations. One to convert the signal into the baseband, and the second to remove the effect of the mode reversal.

<sup>1</sup>Earlier, we defined this quantity as  $\frac{\omega_{ox}^2 - \omega_{oy}^2}{2\omega_{ox}}$ , which is almost equal to  $\omega_{ox} - \omega_{oy}$  if  $\omega_{ox} \approx \omega_{oy}$ .

The first demodulation requires extremely high dynamic range due to the near zero modulation depth. For example,  $10^\circ/\text{hr}$  rate signal with a 100 cps frequency split requires better than 100 ppb amplitude resolution, requiring 24-bit dynamic range, which is essentially impossible.

A force-feedback variant of the LFM gyroscope is also possible. If the amplitude control loops for the two oscillators are sufficiently high bandwidth, then  $\dot{v}_{xa} = \dot{v}_{ya} = 0$  and equations (3.9) and (3.10) become

$$F_{xs} = 2m (\beta_x v_{xao} - (\alpha_z \Omega_z - \Omega_c) v_{yao} \cos \Delta\phi_{xy} - \Omega_{ky} v_{yao} \sin \Delta\phi_{xy}) \quad (4.30)$$

$$F_{ys} = 2m (\beta_y v_{yao} + (\alpha_z \Omega_z + \Omega_c) v_{xao} \cos \Delta\phi_{xy} - \Omega_{kx} v_{xao} \sin \Delta\phi_{xy}). \quad (4.31)$$

The dynamic range requirement is now set by the ratio of rate to resonator bandwidth rather than split frequency. For vacuum packaged devices, bandwidths of less than 1 cps are common. A  $10^\circ/\text{hr}$  rate then translates to approximately a 10 ppm relative change, requiring about 17 bits of dynamic range, a much more realistic specification than required by the displacement measurement.

## 4.5 Impact of amplitude ripple

According to (4.28) and (4.29), the cross-axis spring coupling will cause ripple of the velocity amplitude (if the amplitude control loop is too slow to compensate). This disturbs the quantity  $\Delta r_v$ , thus introduces a rate dependence into  $\Delta\phi_{xy}$ . The effect is difficult to calculate analytically, but numerical simulations show that this introduces a nonlinearity into the rate measurement. As an example, Figure 4.3 shows the effect of this error on a gyroscope with  $\omega_{ox} = 30$  kcps,  $\omega_{oy} = 30.01$  kcps,  $\beta_x = \beta_y = 1$  cps, and  $\Omega_{kx} = 1$  cps. The figure shows the complex envelope components of the measured frequencies. In an ideal LFM gyroscope, the terms  $\dot{\phi}_x \sin \Delta\phi_{xy}$  and  $\dot{\phi}_y \sin \Delta\phi_{xy}$  would lie on top of each other with a constant slope of 1/2, and the terms  $\dot{\phi}_x \cos \Delta\phi_{xy}$  and  $\dot{\phi}_y \cos \Delta\phi_{xy}$  would have a slope of zero. It is evident from the plot that addition of the two measured frequencies acts to correct the nonlinearity, but it would be best to attempt to cancel this effect from the beginning.

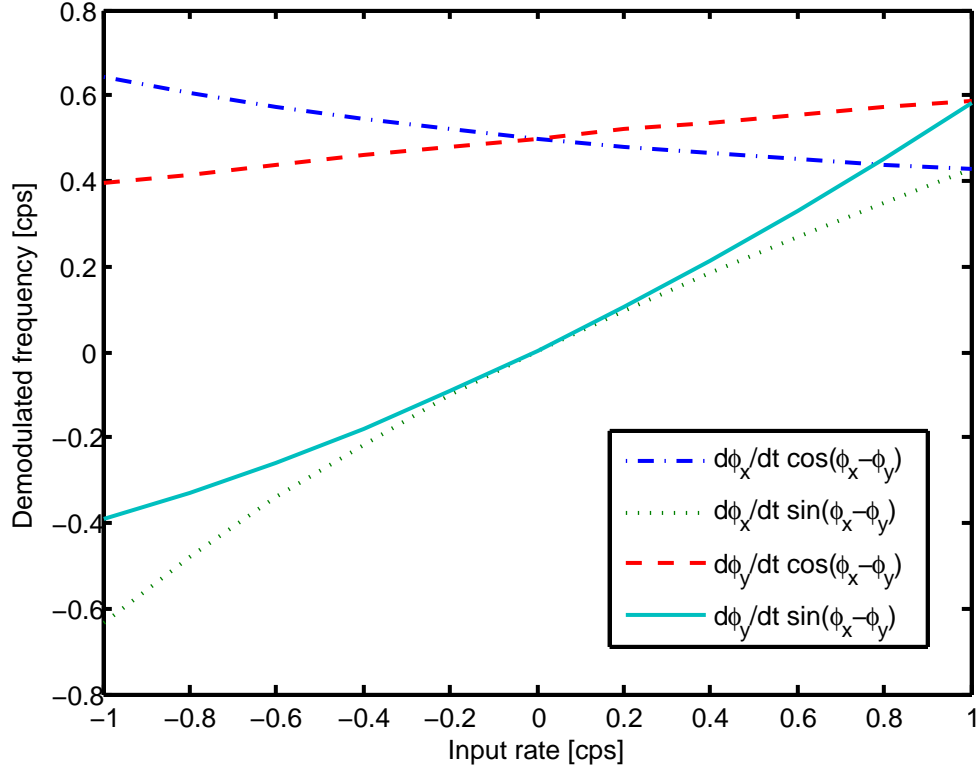


Figure 4.3: Impact of amplitude ripple due to cross-axis spring coupling on LFM gyroscope.

One possibility to eliminate the amplitude ripple is to increase the bandwidth of the amplitude controller. However, designing fast, stable amplitude control loops is problematic due to the complex dynamics of the mode-mismatched gyroscope. Figure 4.4 shows an alternative quadrature cancellation method. The resulting baseband forces implied by Figure 4.4 are

$$F_{xc} = k_{aq}y_a \cos \Delta\phi_{xy} \quad (4.32)$$

$$F_{xs} = k_{ax}x_a - k_{aq}y_a \sin \Delta\phi_{xy} \quad (4.33)$$

$$F_{yc} = k_{aq}x_a \cos \Delta\phi_{xy} \quad (4.34)$$

$$F_{ys} = k_{ay}y_a - k_{aq}x_a \sin \Delta\phi_{xy}. \quad (4.35)$$

The oscillation is sustained by the gain blocks  $k_{ax}$  and  $k_{ay}$ . The multiplication by  $j$  adds the required  $90^\circ$  phase shift between the displacement and force. The values of gain needed are found from (3.5) and (3.6) as  $k_{ax} \approx 2m\beta_x\omega_{ox}$  and  $k_{ay} \approx 2m\beta_y\omega_{oy}$ . In

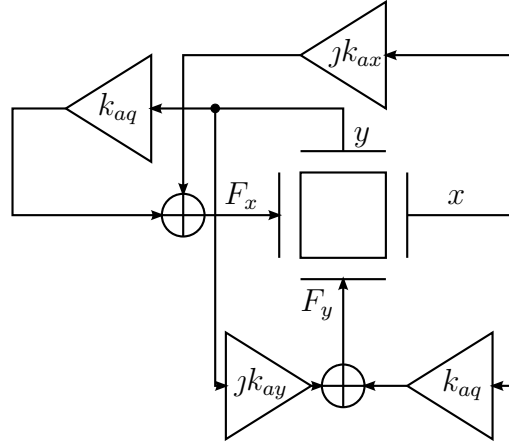


Figure 4.4: Quadrature cancellation method also showing sustaining amplifiers.

practice, these blocks are implemented with variable gain amplifiers. An amplitude controller adjusts the gain in order to achieve the desired displacement set-point.

The quadrature is canceled by the two gain blocks  $k_{aq}$ . Again using (3.5) and (3.6), the required gain is  $k_{aq} = 2m\Omega_{ky}\omega_{oy} = 2m\Omega_{kx}\omega_{ox} = k_{xy}$ . The quadrature can be continuously estimated from multiplication of (4.17) by  $\cos \Delta\phi_{xy}$ . The gain  $k_{aq}$  is adjusted to null this observed quantity. Figure 4.5 shows the demodulated frequencies after the quadrature cancellation.

## 4.6 Gyroscope test bench

Figure 4.6 shows a photograph of the gyroscope test bench. It consists of a rate table, FPGA controller, test board, and gyroscope daughter board. The rate table is an Ideal Aerosmith model 1270VS with a custom controller. A laptop running LabView is mounted on top of the PXI chassis. The PXI chassis containing the FPGA is mounted on top of the laptop and powered through slip-rings. The test board is mounted on top of the PXI and is connected to a gyroscope daughter-board which contains the device under test. The laptop provides local data storage and post-processing and is accessible via WiFi for external control. The system allows for the characterization of the gyroscope scale factor as well as bias.

Figure 4.7 shows the front panel of the FPGA controller. The controller is imple-

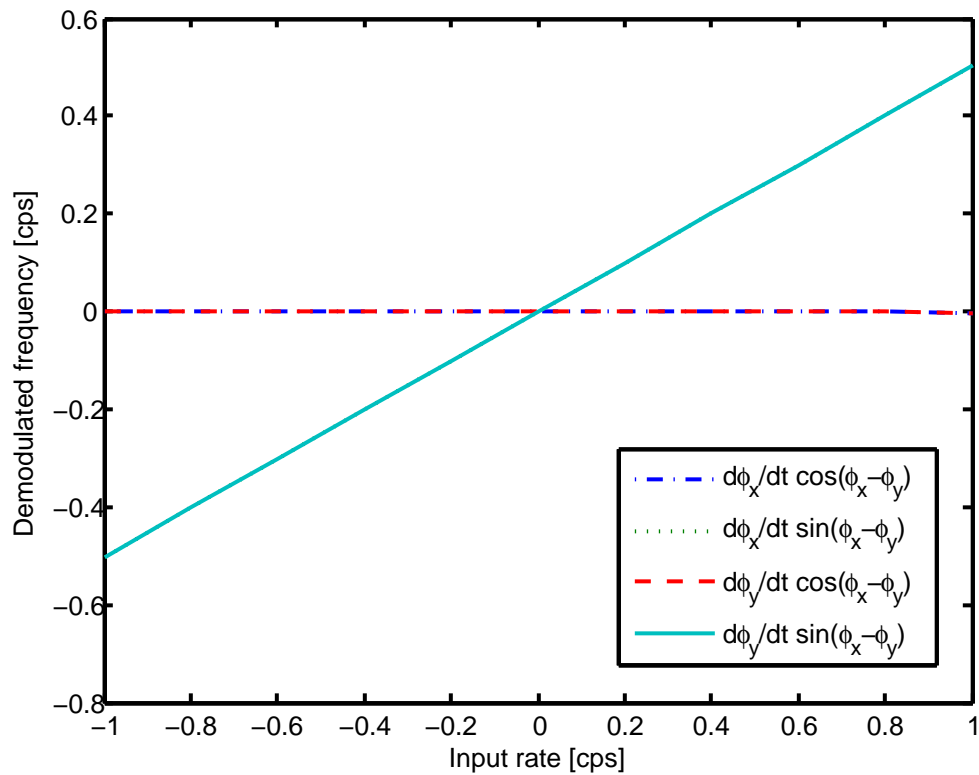
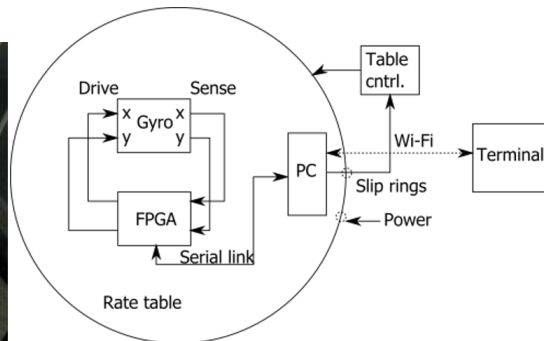
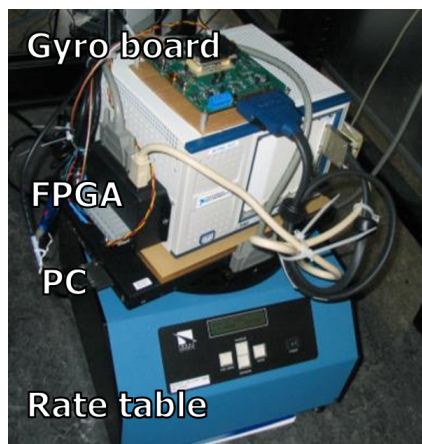


Figure 4.5: Demodulated complex envelope of frequencies after quadrature cancellation.



<b>FPGA</b>	Implements control algorithms: open-loop, mode-reversal, etc.
<b>PC</b>	Data logging
<b>Terminal</b>	User interface

Figure 4.6: Photograph of gyroscope test bench.

mented LabView FPGA, and the front panel is written in LabView. The controller runs on a National Instruments R-series FPGA card (PXI-7854R), which includes 8 analog inputs and 8 analog outputs. The front panel allows the user to select how the analog inputs and outputs connect to the controller, as well as many internal configuration options. The *LIA input select* section configures how the analog inputs connect to the lock-in amplifier (LIA) modules. Each LIA consists of a PLL (Costas loop) and a I/Q demodulator. The *PLL Configuration* section sets the center frequency and bandwidth of the PLLs. The *Demod Config* section selects which clocks, generated by the PLLs, should be used to demodulate which input channels. For example, a clock locked to input channel 1 could be used to I/Q demodulate an input connected to channel 2. Additionally, the bandwidth of the I/Q demodulator and the amount of decimation are configurable.

The *PI controller config* section sets the proportional and integral gain and set point of the 8 PI controllers. Each PI controller is attached to either the in-phase or the quadrature component of the input channel. Additionally, the PI controller reference can be configured to be a sinusoid instead of a constant value. The frequency, amplitude, and phase (relative to PLL reference) of the sinusoid are configurable. The PIs control the slowly varying components of the sinusoidal inputs. For example, the PIs can be used to sustain constant envelopes of the high frequency input signal, or AM modulation of the input signal. The *Output Mux* section selects the output that the PI controller affects. The selected PI control signal is then modulated back to the carrier frequency by an I/Q modulator which is synchronous with the particular I/Q demodulator reference.

## 4.7 Dual mass gyroscope test chip

The Lissajous pattern gyroscope operation was first demonstrated on a 3.3 kcps pendular gyroscope fabricated by Invensense. Figure 4.9 shows a photograph of the transducers, and Figure 4.10 shows a die photo. The die is approximately 5 by 3 mm<sup>2</sup> and is bonded to an LCC-44 package. Each transducer consists of a 1 mm by 1 mm proof mass suspended by folded flexures. Drive and sense combs surround the proof

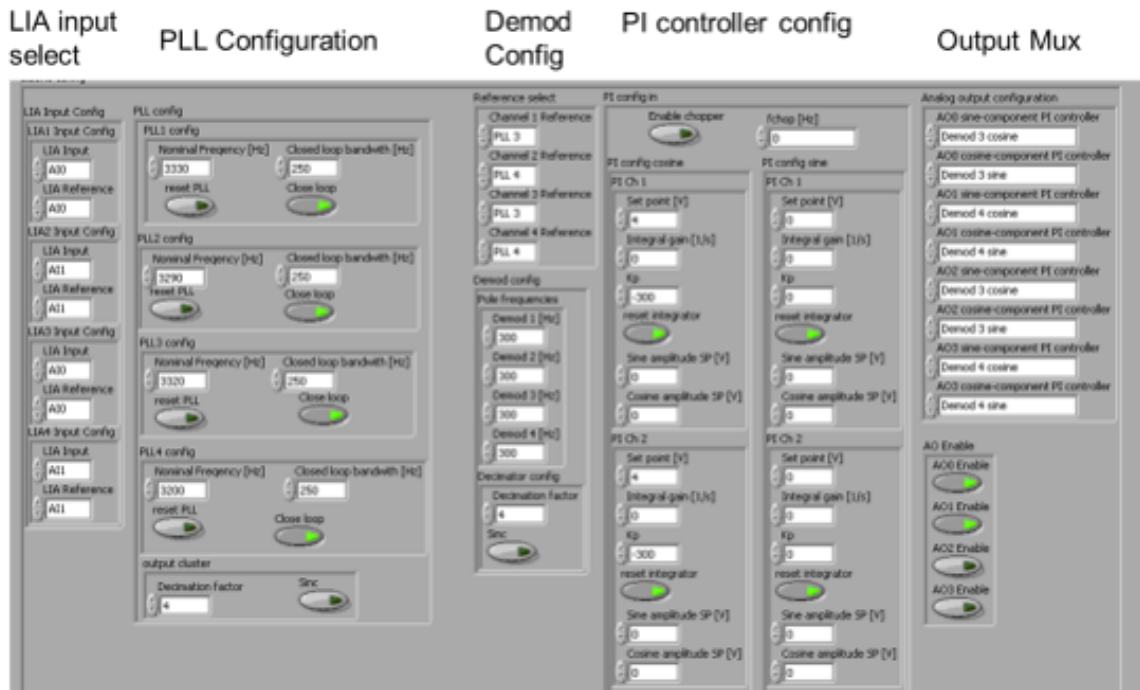


Figure 4.7: Front panel of FPGA controller.

mass. They are located in frames which are coupled to only one direction of proof mass motion. The springs in the interior of the mass decouple the frames from motion in the orthogonal direction. The folded flexures surrounding the frames anchor the structure and contribute to the stiffness of the translational modes. The design is nominally symmetric, but small mismatches between the modes enable LFM operation.

Figure 4.8 shows the measured frequency response of the x- and y-axes. The resonant frequencies of the representative device are approximately 3.379 kcps and 3.405 kcps, giving a nominal frequency split of  $\Delta\omega_o = 26$  kcps. The bandwidth of the modes is approximately  $\beta = 1.7$  cps.

A CMOS readout ASIC was designed along with the mechanical transducer. Figure 4.11 shows a layout diagram of the CMOS die, and Figure 4.12 shows a partial schematic of the included electronics. Each axis of of the gyroscope is buffered by a low-noise, fully-differential transcapacitance amplifier which produces a signal in phase with the displacement of the mechanical transducer. The chip includes chop-

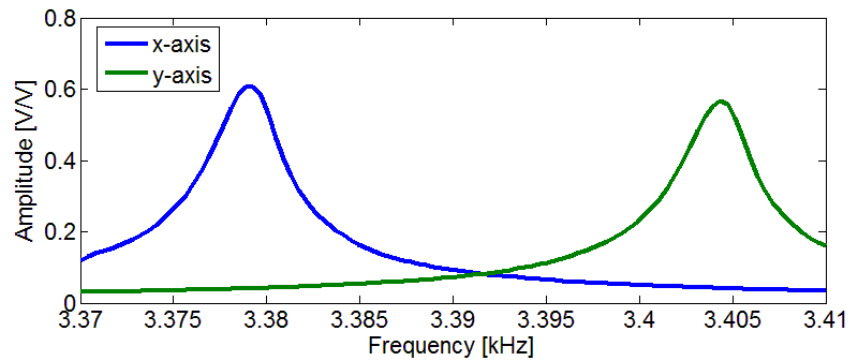


Figure 4.8: Representative frequency response of dual mass gyroscope.

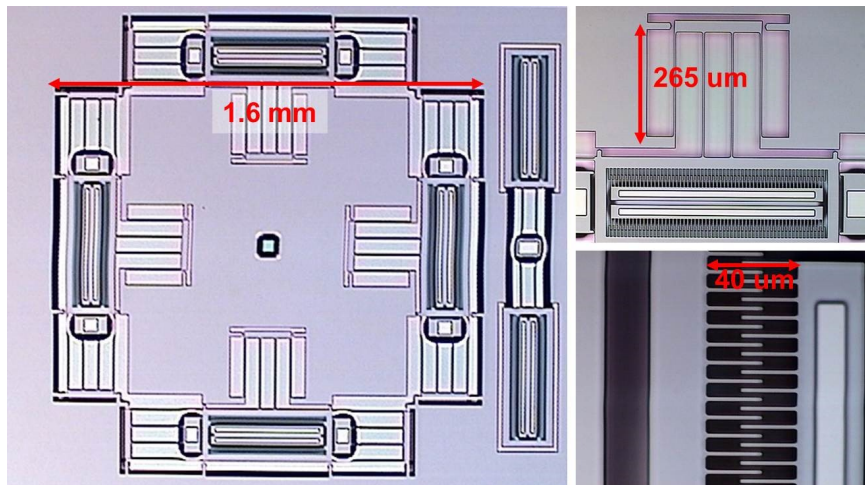


Figure 4.9: Picture of 3.3 kcps pendular gyroscope fabricated by Invensense.

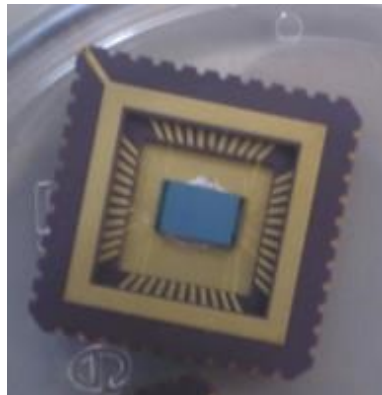


Figure 4.10: Die photo of test chip.

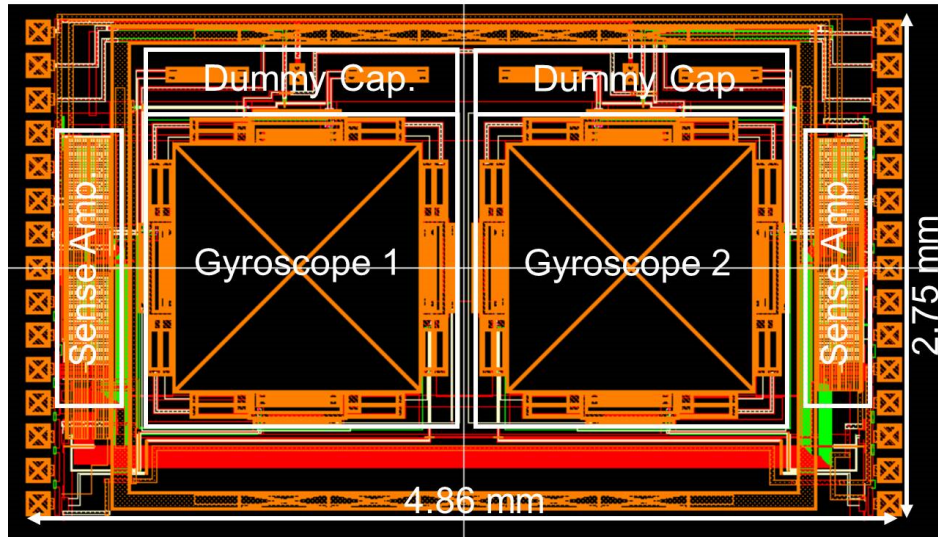


Figure 4.11: Layout diagram of 3.3 keps pendular gyroscope fabricated by Invensense.

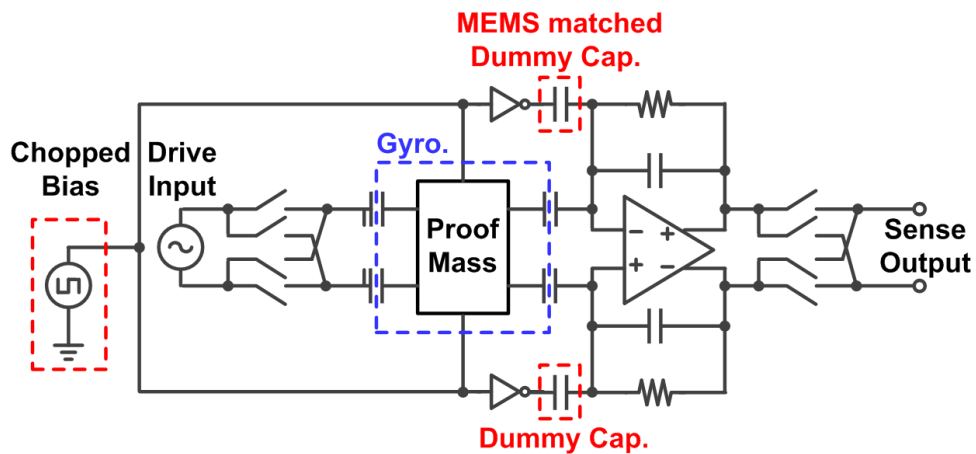


Figure 4.12: Partial schematic of readout electronics for 3 keps pendular gyroscope.

per switches for modulating the proof mass bias. This overcomes flicker noise that would otherwise dominate the circuit noise at 3 keps. The MEMS dummy caps are used to cancel common-mode feedthrough from the proof mass chopping signal. A chopper demodulator is included on the chip and follows the transcapacitance amplifier.

## Dual Force Feedback Operation

The amplitude modulated modes of operation were discovered before the frequency readout [18]. The original concept was to create a dual force feedback gyroscope in which both axes were continuously excited. By (4.31), this is possible if the axes are driven in quadrature with one another.

The dual force-feedback controller is implemented with the above described FPGA controller. Figure 4.13 shows the controller configuration for dual force feedback operation. The desired proof mass trajectory is obtained through single-sideband (SSB) amplitude modulation of the displacement signals relative to the carrier  $\cos(\omega_o t)$ . The carrier is obtained from a phase-locked loop connected to a replica MEMS oscillator on the same substrate. The x-axis is lower sideband modulated with  $\cos(\omega_c t)$  and the y-axis is upper sideband modulated with  $\sin(\omega_c t)$ . This results in a Lissajous pattern: constant and equal envelope oscillations on both the x- and y-axes, with a frequency difference equal to  $\omega_c$ .

The baseband forcing signals generated by the PID controllers are demodulated with respect to the chopping references and are combined to form the rate estimate. Most of the bias errors are rejected after demodulation, including frequency mismatch between the carrier and resonant frequencies, quadrature error, and cross-damping error.

Only one of the two gyroscopes is used for sensing angular rate. The second gyroscope serves as a clock reference for generating the frequency  $\omega_o$ . This clock tracks the first gyroscopes resonant frequency variations, further attenuating residual bias errors.

Figure 4.14 shows the Allan deviation obtained in the dual force-feedback operating mode. The Allan deviation is compared to the same test run in the single force feedback mode for reference. The long term performance of the gyroscope is greatly improved, as the averaging limit is not reached until 4348 s. However, the short term performance of the gyroscope is worse than the single force-feedback mode. This is for several reasons. First, the gyroscope is not operating at either mechanical resonance. The oscillations are sustained at frequencies determined by the second

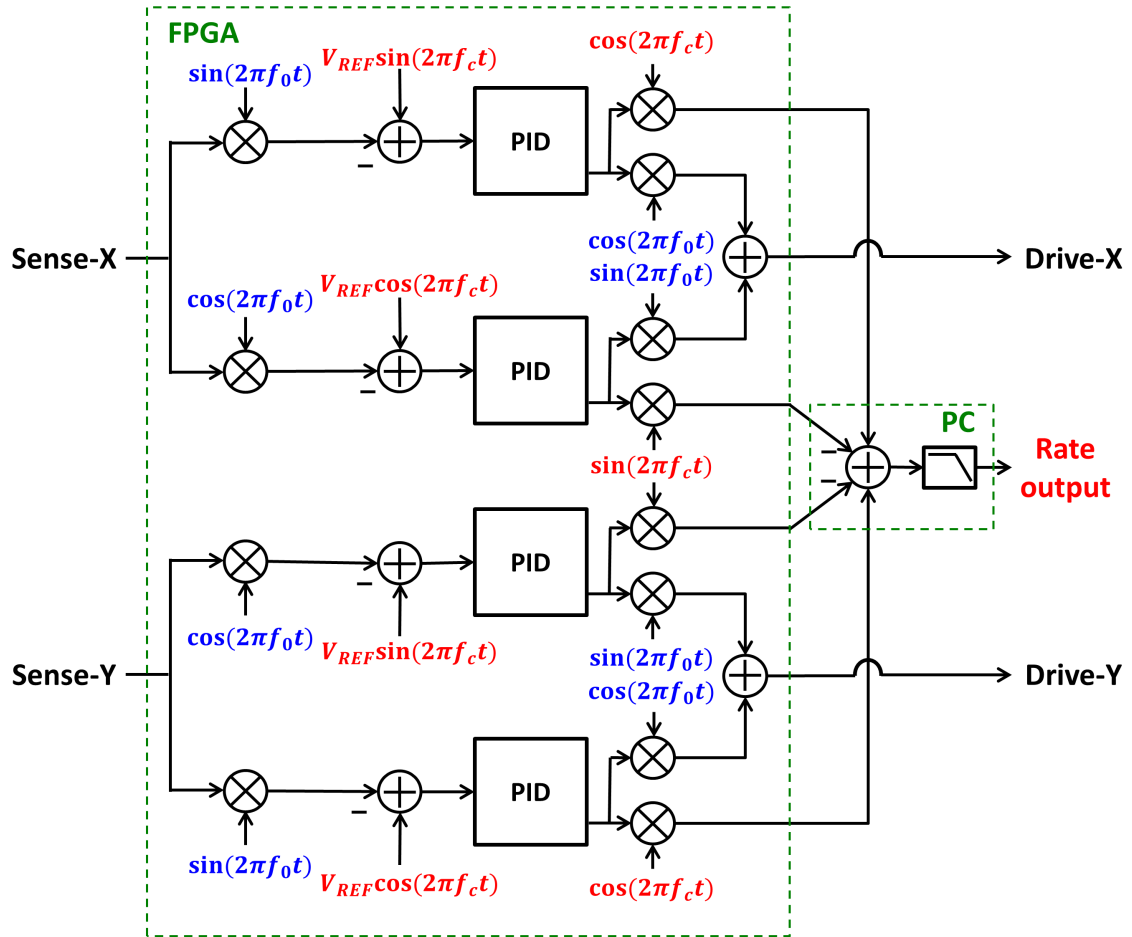


Figure 4.13: Dual force-feedback gyroscope controller implementation.

reference oscillator and the baseband controller. Second, as explained in Section 4.4 the dual force-feedback operating mode requires a measurement of forces with extremely high dynamic range. These two problems limit the application of the dual force-feedback operating mode, but each of these limitations can be overcome with frequency readout.

## LFM Operation

LFM operation is demonstrated using the dual mass pendular gyroscope described above. Figure 4.15 shows a conceptual implementation of the LFM gyroscope. Two

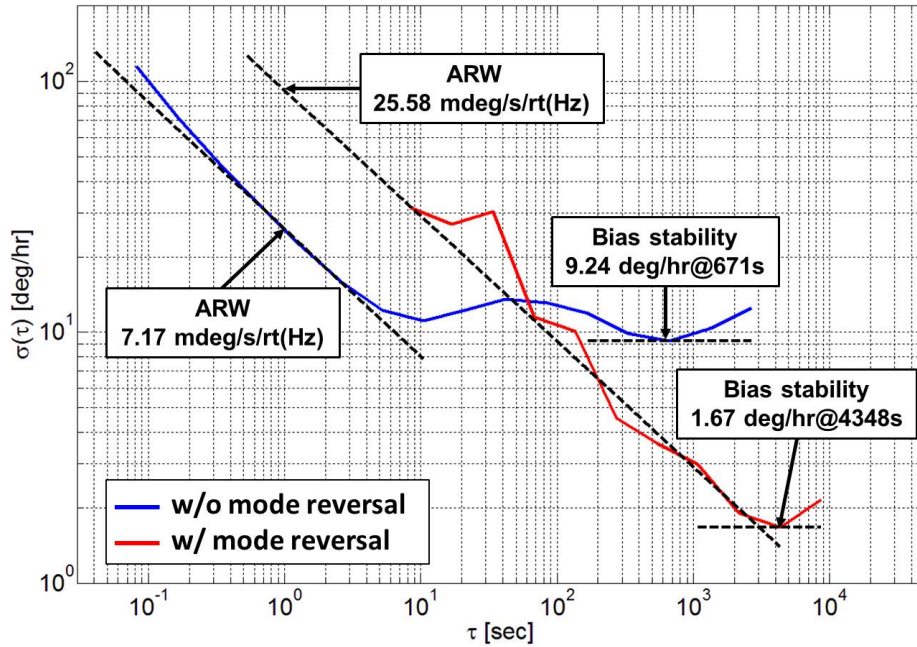


Figure 4.14: Comparison of Allan Deviation for conventional force feedback and dual force feedback (Lissajous pattern) operating modes.

oscillators maintain equal, constant velocity amplitude oscillations on each axis at their respective natural frequencies. Optionally, a split frequency controller is used to tune the frequency split. The frequencies of each axis are measured by the frequency demodulators, and the signal is passed to the LFM demodulator of Figure 4.16.

The LFM demodulator extracts the component of the oscillation frequency which is in phase with the sine of the phase difference between the two oscillations. A synchronous AM demodulator multiplies the measured frequency by the extracted demodulator reference to form the bias-free rate estimate. The demodulator reference is found directly from the oscillation signals by, for example, multiplying them together and low pass filtering.

The controller is implemented with the same FPGA hardware described for the dual force-feedback gyroscope. In the frequency readout configuration, the PLLs in combination with two PI controllers maintain equal, constant envelope oscillations on each axis. The PLLs provide a measure of the frequency of oscillation relative to

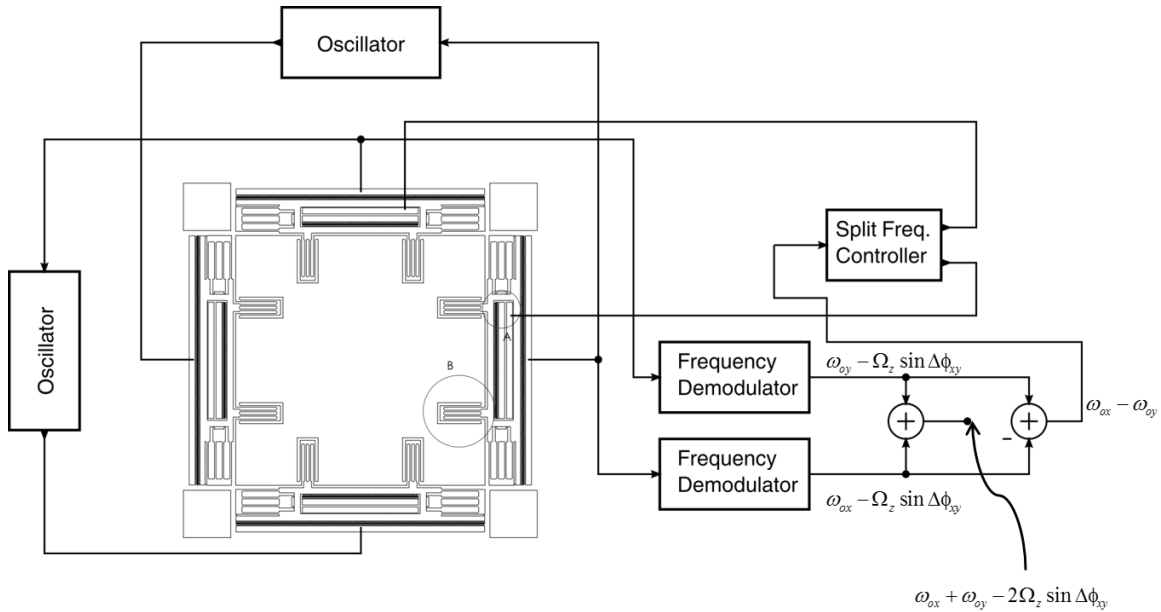


Figure 4.15: Conceptual implementation of LFM gyroscope. The split frequency controller is optional.

a 10 Mcps reference.

Figure 4.17 shows the raw input-output relationship of the rate sensor. The uncalibrated scale factor is approximately 0.95 cps/cps, or  $\alpha_z \approx 0.95$ . The sensor maintains excellent linearity throughout the  $\pm 90^\circ/\text{s}$  input range, limited by the measurement setup. Figure 4.18 shows the relative error from the ideal transfer function, which is less than 40 ppm across the input range.

The LFM gyroscope bias and scale factor were characterized across temperature and compared to the conventional AM gyroscope. Figure 4.19 shows the baseline AM performance. The two steps correspond to temperature changes from  $25^\circ\text{C}$  to  $45^\circ\text{C}$  and back to  $25^\circ\text{C}$ . The temperature coefficients are  $11.2 \times 10^{-3}^\circ/\text{s}/\text{K}$  for the bias and 4100 ppm/K for the scale factor. A similar test is conducted for the LFM operating mode. The bias and scale factor coefficients improve to  $2.4 \times 10^{-3}^\circ/\text{s}/\text{K}$  and 27 ppm/K, respectively, or relative improvements by factors of 4.6 and 152.

The bias stability improvement is largely due to the rejection of cross damper error. The cross damper error contributes offset in opposite directions on each axis, and the addition cancels the drift. The scale factor improvement is due to the inherent

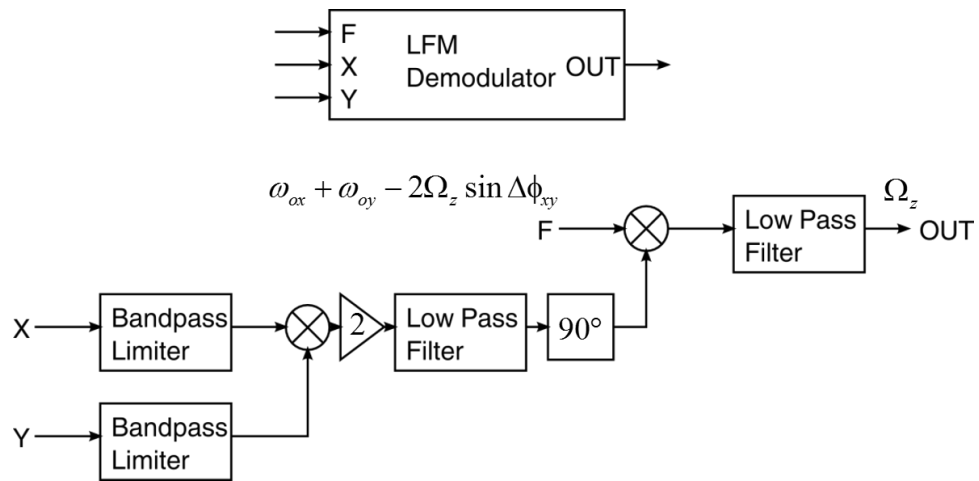


Figure 4.16: Conceptual implementation final LFM demodulation. The measured frequencies are further AM demodulated in order to form the bias-free rate estimate.

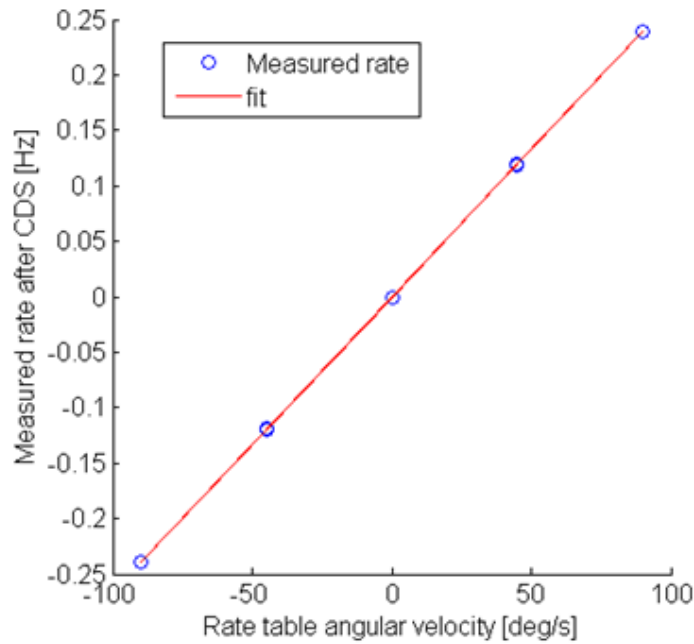


Figure 4.17: Uncalibrated output of gyroscope showing accurate scale factor of LFM operating mode.

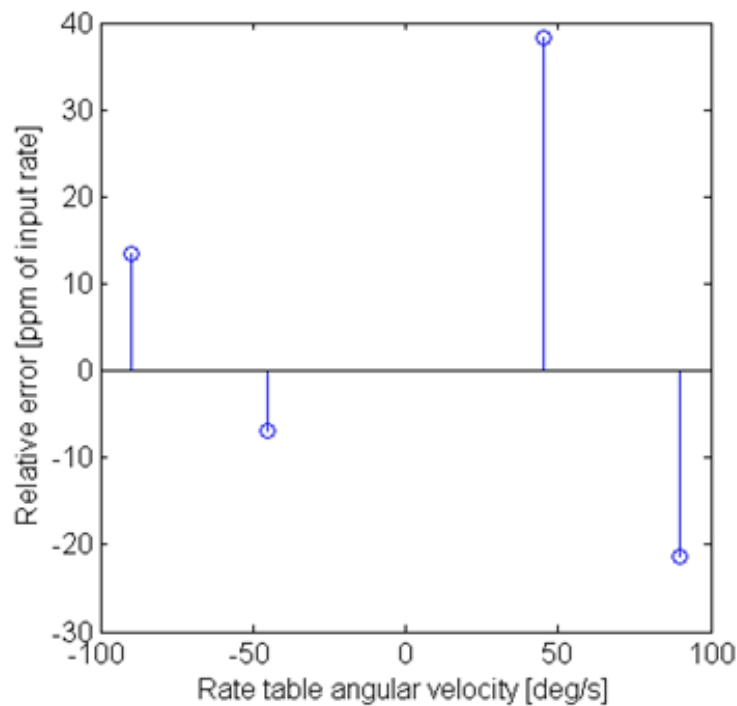


Figure 4.18: Deviation from the ideal linear transfer curve in the LFM operating mode.

stability of a term that is the sum of reciprocal fractions, as described in Section 3.3.

Long term bias stability tests were carried out for the LFM operating mode. A gyroscope was placed in the test bench on January 30, 2013, calibrated, and left until April 8, 2013, and a measurement of the gyroscope's bias was recorded on several days in between. The bias is measured by averaging for a few hundred seconds, which reduces the noise variance enough to observe the long term drift. Figure 4.21 shows the measured gyro bias. The bias is less than  $\pm 60$  ppm relative to  $1000^\circ/\text{s}$ , or  $60 \times 10^{-3}^\circ/\text{s}$ .

The scale factor of the device is also characterized over a few days in ambient conditions and compared to the conventional AM operating mode. Figure 4.22 shows the relative scale factor variation of the AM mode. The peak-to-peak variation is greater than 36,000 ppm, or 3.6%. Figure 4.23 shows the scale factor variation over a day in the LFM operating mode. The variation is less than 100 ppm, a factor of over

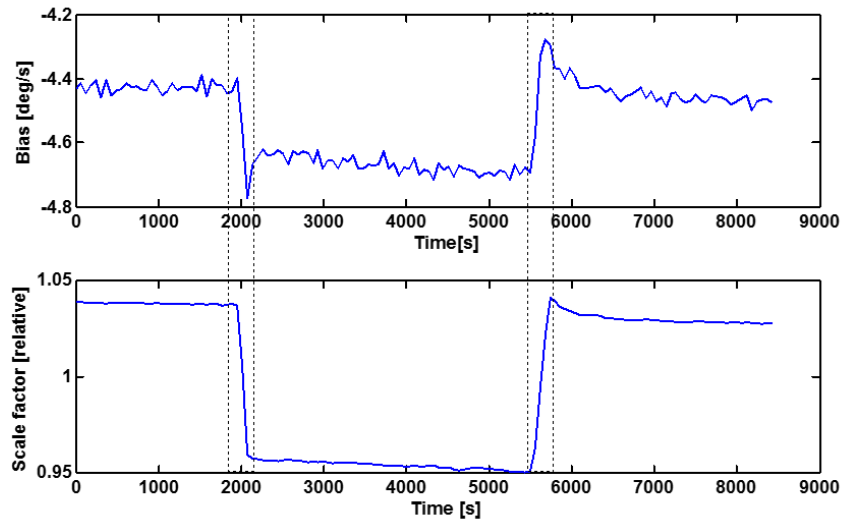


Figure 4.19: Bias and relative scale factor response to a temperature step in the open loop rate mode. The steps correspond to 20 K shifts. The bias coefficient is  $11.2 \times 10^{-3} \text{ }^\circ/\text{s/K}$ , and the scale factor is 4100 ppm/K.

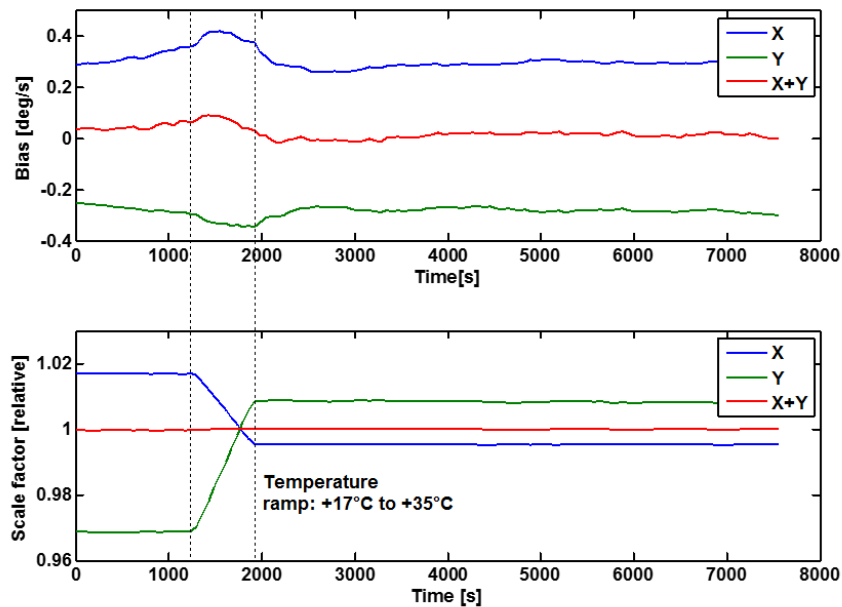


Figure 4.20: Bias and relative scale factor response to a temperature step in the LFM mode. The bias coefficient is  $2.4 \times 10^{-3} \text{ }^\circ/\text{s/K}$ , and the scale factor is 27 ppm/K.

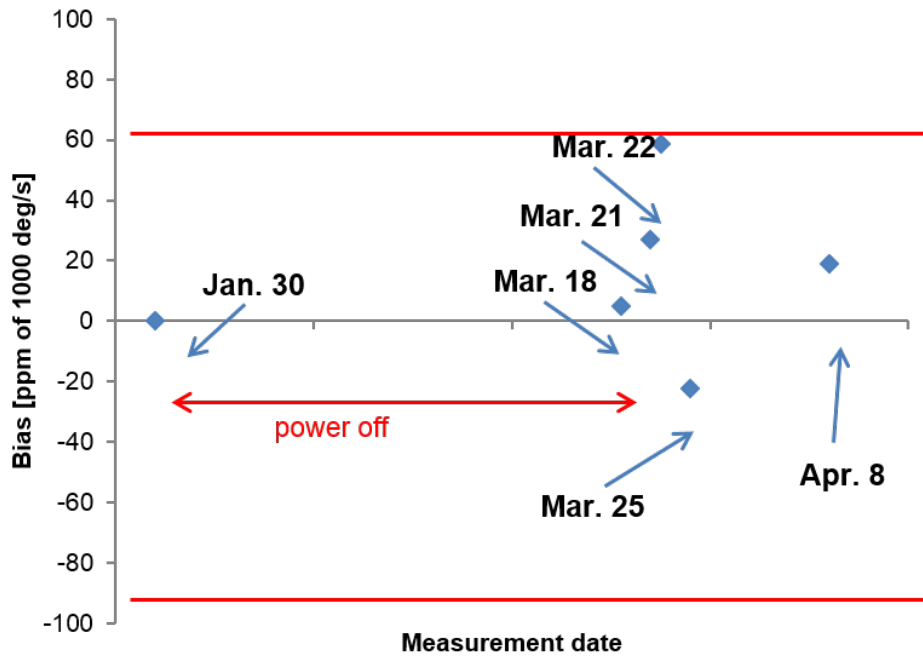


Figure 4.21: The long term bias over a few months is less than  $\pm 60$  ppm relative to  $1000^\circ/\text{s}$ , or  $60 \times 10^{-3}^\circ/\text{s}$ .

360 improvement.

## 4.8 Conclusion

The dual mass gyroscope test chip proves the concept of the Lissajous pattern gyroscope. The dual force-feedback operating mode shows the best bias stability, achieving sub-2 deg/hr at about 1 hour averaging time. The LFM operating mode shows drastic scale factor reliability improvements of over 2 orders of magnitude, as well large factors of improvement in the long term bias stability.

Table 4.1 displays a comparison of the AM and FM gyroscope operating modes. As opposed to the AM gyroscopes, the FM gyroscopes offer a scale factor which is independent of both frequency mismatch and resonator bandwidth. Additionally, the LFM gyroscope rejects the cross-damper error  $\Omega_c$  and the quadrature error  $\Omega_k$ .

The LFM operating mode promises to improve long term scale factor stability,

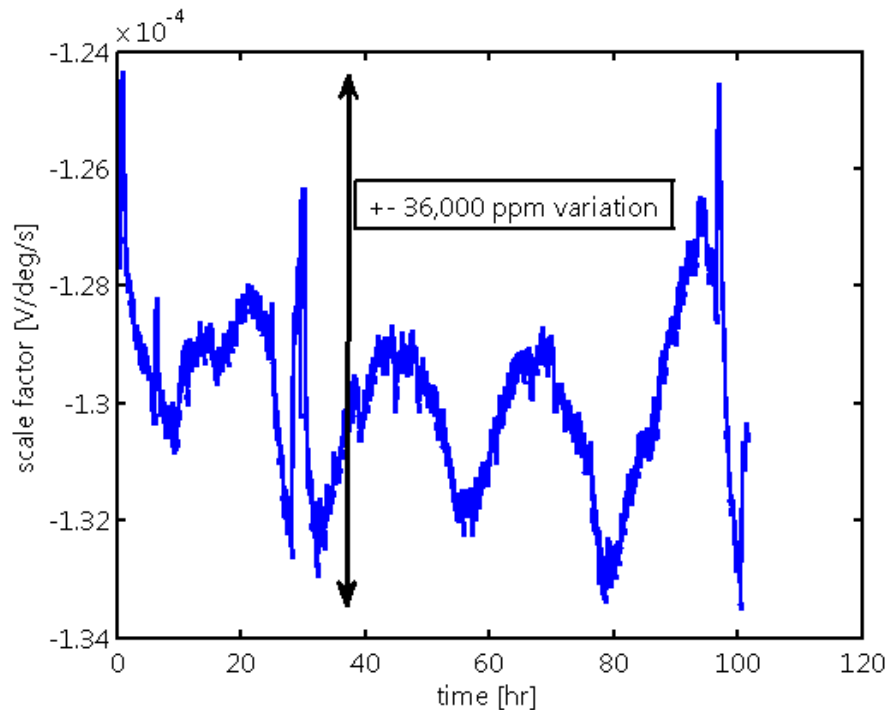


Figure 4.22: Scale factor variation over 3 days in the conventional AM operating mode.

long term bias stability, and power consumption of MEMS gyroscopes. The former property is due to a scale factor that only depends on the mechanical angular gain to first order. The improved bias stability is due to the effective mode-reversal, or periodic orbital direction switching. The lower power consumption is possible because the LFM gyroscope can operate at frequency splits much smaller than the conventional AM gyroscope, without sacrificing scale factor stability.

The above benefits make the LFM operating mode an attractive option for further improvement of MEMS vibratory gyroscopes.

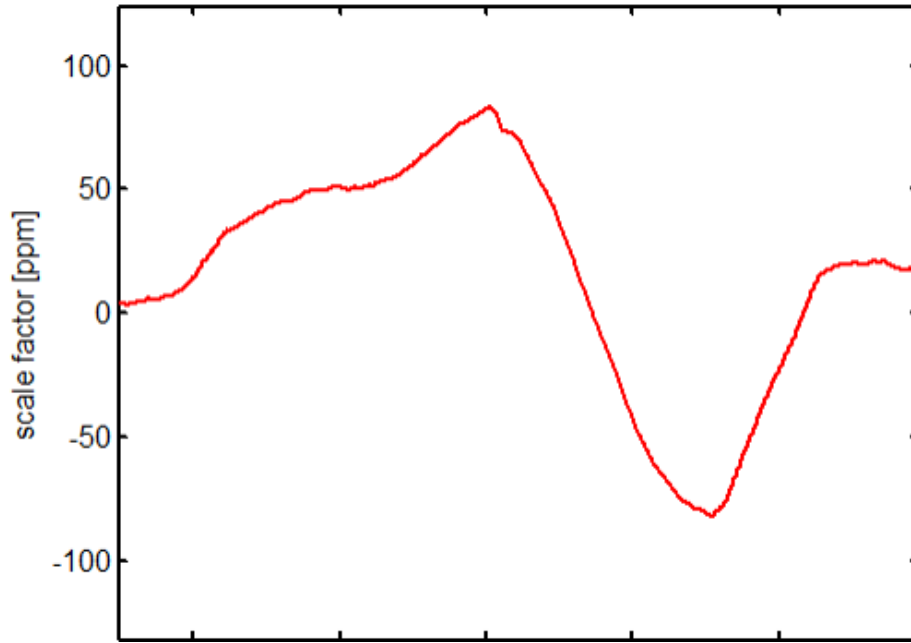


Figure 4.23: Scale factor variation over 1 day in LFM operating mode. The x-axis scale is 6 hours per division.

	AM (Conventional)		FM	
Mode Matched	No	Yes	No (LFM)	Yes (QFM)
Bandwidth	$\Delta\omega_o$	$\beta$	$\Delta\omega_o$	unrestricted
Scale factor	$\frac{\alpha_z}{\Delta\omega_o}$	$\frac{-\alpha_z\beta}{\beta^2 + \Delta\omega_o^2}$	$-\frac{1}{2}\alpha_z\Sigma r_v$	$-\alpha_z\Sigma r_v$
Offset	$\frac{1}{\alpha_z} \left( \Omega_c - \Omega_k \frac{\beta}{\Delta\omega_o} \right)$	$\frac{\Omega_c}{\alpha_z}$	$\frac{\Omega_c}{\alpha_z} \Delta r_v$	$-\frac{\omega_c + \Omega_c}{\alpha_z}$
Rate noise (ratio to mode matched)	$\frac{\Delta\omega_o}{\beta}$	1	$\frac{\Delta\omega_o}{\beta}$	1

Table 4.1: Comparison of scale factor and offset of AM and FM gyroscopes.

# Bibliography

- [1] G. A. Wilkins, “The IAU style manual,” *IAU Transactions*, vol. XXB, no. 5, 1989.
- [2] “IEEE standard specification format guide and test procedure for single-axis laser gyros,” *IEEE Std 647-1995*, 1995.
- [3] D. B. Sullivan, D. W. Allan, D. A. Howe, and F. L. Walls, “Characterization of clocks and oscillators,” *NIST Technical Note 1337*, 1990.
- [4] J. Rutman, “Characterization of phase and frequency instabilities in precision frequency sources: Fifteen years of progress,” *Proceedings of the IEEE*, vol. 66, no. 9, pp. 1048–1075, 1978.
- [5] J. A. Geen, S. J. Sherman, J. F. Chang, and S. R. Lewis, “Single-chip surface-micromachined integrated gyroscope with 50/hour root allan variance,” in *Solid-State Circuits Conference, 2002. Digest of Technical Papers. ISSCC. 2002 IEEE International*, vol. 1, pp. 426–427 vol.1.
- [6] C. Byoung-doo, P. Sangjun, K. Hyoungho, P. Seung-Joon, P. Yonghwa, L. Geunwon, L. Ahra, L. Sang Chul, W. Carr, D. Setiadi, R. Mozulay, and C. Dong-II, “The first sub-deg/hr bias stability, silicon-microfabricated gyroscope,” in *Solid-State Sensors, Actuators and Microsystems, 2005. Digest of Technical Papers. TRANSDUCERS '05. The 13th International Conference on*, vol. 1, pp. 180–183 Vol. 1.

- [7] M. Saukoski, L. Aaltonen, and K. A. I. Halonen, “Zero-rate output and quadrature compensation in vibratory mems gyroscopes,” *Sensors Journal, IEEE*, vol. 7, no. 12, pp. 1639–1652, 2007.
- [8] E. Tatar, S. E. Alper, and T. Akin, “Effect of quadrature error on the performance of a fully-decoupled mems gyroscope,” in *Micro Electro Mechanical Systems (MEMS), 2011 IEEE 24th International Conference on*, pp. 569–572.
- [9] Y. Bo, Z. Bailing, W. Shourong, H. Libin, and Y. Yong, “A quadrature error and offset error suppression circuitry for silicon micro-gyroscope,” in *Nano/Micro Engineered and Molecular Systems, 2008. NEMS 2008. 3rd IEEE International Conference on*, pp. 422–426.
- [10] A. Sharma, M. F. Zaman, and F. Ayazi, “A 0.2/hr micro-gyroscope with automatic cmos mode matching,” in *Solid-State Circuits Conference, 2007. ISSCC 2007. Digest of Technical Papers. IEEE International*, pp. 386–610.
- [11] L. Prandi, C. Caminada, L. Coronato, G. Cazzaniga, F. Biganzoli, R. Antonello, and R. Oboe, “A low-power 3-axis digital-output mems gyroscope with single drive and multiplexed angular rate readout,” in *Solid-State Circuits Conference Digest of Technical Papers (ISSCC), 2011 IEEE International*, pp. 104–106.
- [12] D. D. Lynch, “Vibratory gyro analysis by the method of averaging,” in *2nd Saint Petersburg International Conference on Gyroscopic Technology and Navigation Part I*, 1995, pp. 26–34.
- [13] C. D. Ezekwe and B. E. Boser, “A mode-matching  $\Sigma\Delta$  closed-loop vibratory gyroscope readout interface with a  $0.004^\circ/\text{s}/\sqrt{\text{Hz}}$  noise floor over a 50 Hz band,” *IEEE Journal of Solid-State Circuits*, vol. 43, no. 12, pp. 3039–3048, 2008.
- [14] M. H. Kline, Y. Yeh, B. Eminoglu, H. Najar, M. Daneman, D. A. Horsley, and B. E. Boser, “Quadrature fm gyroscope,” in *Micro Electro Mechanical Systems (MEMS), 2013 IEEE 26th International Conference on*, pp. 604–608.

- [15] J. Seeger, M. Lim, and S. Nasiri, “Development of high-performance, high-volume consumer mems gyroscopes,” in *Solid-State Sensors, Actuators, and Microsystems Workshop*, 2010, pp. 61–64.
- [16] S. F. Wyse and R. E. Stewart, “Vibratory gyro bias error cancellation using mode reversal,” 2011, (US) [US] 7350412; 7350414.
- [17] R. E. Stewart and S. F. Wyse, “Bias and quadrature reduction in class ii coriolis vibratory gyros,” 2009, (US) [US] 7350412; 7350413.
- [18] M. Kline, Y.-C. Yeh, B. Eminoglu, I. Izyumin, M. Daneman, D. Horsley, and B. Boser, “Mems gyroscope bias drift cancellation using continuous-time mode reversal,” in *Solid-State Sensors, Actuators and Microsystems (TRANSDUCERS EUROSENSORS XXVII), 2013 Transducers Eurosensors XXVII: The 17th International Conference on*, 2013, pp. 1855–1858.